Quaternary Science Reviews 288 (2022) 107593

Contents lists available at ScienceDirect

Quaternary Science Reviews

journal homepage: www.elsevier.com/locate/quascirev

Invited review

A review of orbital-scale monsoon variability and dynamics in East Asia during the Quaternary

Youbin Sun [a, b, e, *], Ting Wang [a, c], Qiuzhen Yin [d], Anqi Lyu [d], Michel Crucifix [d], Yanjun Cai [e], Li Ai [a], Steven Clemens [f], Zhisheng An [a, b, g]

[a] State Key Laboratory of Loess and Quaternary Geology, Institute of Earth Environment, Chinese Academy of Sciences, Xi'an, China
[b] Center for Excellence in Quaternary Science and Global Change, Chinese Academy of Sciences, Xi'an, China
[c] University of Chinese Academy of Sciences, Beijing, China
[d] Georges Lemaître Center for Earth and Climate Research, Earth and Life Institute, Université Catholique de Louvain, Louvain-la-Neuve, Belgium
[e] Institute of Global Environmental Change, Xi'an Jiaotong University, Xi'an, China
[f] Department of Earth, Environmental and Planetary Sciences, Brown University, Providence, USA
[g] Open Studio for Oceanic-Continental Climate and Environment Changes, Pilot National Laboratory for Marine Science and Technology, Qingdao, China

ARTICLE INFO

Article history:
Received 13 December 2021
Received in revised form
28 May 2022
Accepted 29 May 2022
Available online 10 June 2022

Handling Editor: Yan Zhao

Keywords:
East Asia
Quaternary monsoon change
Proxy records
Modeling results
Orbital-scale monsoon dynamics

ABSTRACT

Quaternary monsoon changes in East Asia have been extensively investigated by proxy records from continental and marine archives. However, these proxy indicators often show controversial characteristics in terms of trends and rhythms, leading to perplexedunderstanding of orbital-scale monsoon dynamics. Here we review the orbital-scale monsoon variability and dynamics in East Asia by comparing multiple proxies from loess, lake, speleothem, and marine records with the HadCM3 modeling result. Evolutionary power spectra of loess grain size and sea surface temperature exhibit a remarkable shift from 41- to 100-kyr cycles across the mid-Pleistocene transition (MPT), whereas other proxy records (e.g. $\delta^{13}C$ of loess carbonate, pollen concentration in lake sediments, and magnetic mineral compositions in marine sediments) display distinct and persistent precession cycles through the Quaternary, along with strong 100-kyr cycles after the MPT. Simulations with the HadCM3 climate model reveal that the effects of orbital parameters, ice volume, and CO_2 concentration on the temperature, precipitation, and southerly winds are seasonally and spatially different in East Asia. In the summer season, orbitally induced insolation plays a dominant role in driving changes in these three climate variables except for summer precipitation in south China (20-30°N), whilst annual changes in precipitation and temperature are jointly affected by insolation, ice volume, and CO_2. Proxy-model comparison suggests that several land-based proxies are sensitive to changes in summer precipitation, annual precipitation, and annual temperature, though their responses to astronomical, ice, and CO_2 forcing being quite different between north and south China. Our proxy-model comparison reveals that diverse expression of Quaternary climate periodicities was provoked by different sensitivities of marine and terrestrial proxies to seasonal and/or annual changes in precipitation and temperature, and by different responses of temperature and precipitation to insolation and ice/CO_2 forcing. We suggest that understanding of Quaternary climate change can be deepened by further comparison of quantitatively reconstructed paleotemperature and precipitation data with high-resolution regional climate modeling results.

1. Introduction

Milutin Milankovitch proposed that changes in orbitally induced summer insolation played a key role in driving glacial cycles (Milankovitch, 1941), which was subsequently the basis of what is now termed as the "Milankovitch theory" (Hays et al., 1976; Imbrie and Imbrie, 1979; Berger et al., 1984). The theory suggests that the amount of ice/snow melting during the summer season, induced by incoming solar radiation in the Northern Hemisphere high-latitude region, is a driver or at least a pacemaker of the Quaternary ice-age cycles. Benthic $\delta^{18}O$ records from deep-sea

* Corresponding author. State Key Laboratory of Loess and Quaternary Geology, Institute of Earth Environment, Chinese Academy of Sciences, Xi'an, China.
E-mail address: sunyb@ieecas.cn (Y. Sun).

https://doi.org/10.1016/j.quascirev.2022.107593

sediments have provided robust evidence supporting the Milankovitch theory (Hays et al., 1976; Shackleton and Opdyke, 1976). Spectral analysis of the 2-Myr $\delta^{18}O$ record reveals a notable periodicity shift from 41-kyr before ~1.2 Ma to 100-kyr after ~0.7 Ma (Pisias and Moore, 1981), which has been named the Mid-Pleistocene transition (MPT) (e.g. Ruddiman et al., 1986; Raymo et al., 1997; Clark et al., 2006). Over the past three decades, numerous proxies from deep-sea sediments demonstrate that changes in global ice volume (e.g. Lisiecki and Raymo, 2005), sea level (Rohling et al., 2014), sea surface temperature (Elderfield et al., 2012), and thermohaline circulation (Raymo et al., 1997) all exhibit a periodicity shift from 41-kyr to 100-kyr cycles across the MPT (e.g. Clark et al., 2006; Head and Gibbard, 2015).

In contrast to conventional MPT characteristics of the marine environment, proxy records that reflect Asian monsoonal circulation exhibit strong precession cycles during the mid-to-late Pleistocene (e.g. Wang et al., 2014; An et al., 2015). In the Asian monsoon region, the precession signal is quite similar in periodicity but different in phase between Chinese speleothem and Arabian sea sediments (e.g. Wang et al., 2008; Ziegler et al., 2010; Caley et al., 2011; Cheng et al., 2016), different from the terrestrial monsoon responses to astronomical and glacial forcing being recognized in Chinese loess sediments (e.g. Liu et al., 1999; Ding et al., 2002; Sun et al., 2006a, 2015; Maher, 2016). Most notably, absolutely-dated speleothem $\delta^{18}O$ records in East Asia exhibit prominent 23-kyr precession cycles over the past 640 ka (Wang et al., 2008; Cheng et al., 2016). Hydrologically-related proxies from paleolakes in the Tengger Desert, Heqing and Zoige basins and $\delta^{13}C$ of inorganic carbonate from Jingyuan loess sequence all exhibit strong precession cycles through the Pleistocene (An et al., 2011; Sun et al., 2019; Zhao et al., 2020; Liu et al., 2021). Curiously, however, precession cycles are absent in the late Pleistocene seawater $\delta^{18}O$-based runoff reconstruction from the East China Sea; a record in which the temperature and global ice volume signals have been quantitatively removed (Clemens et al., 2018). Aside from the precession signal, 100-kyr cycles are found in loess grain-size (e.g. Ding et al., 1994, 2002; Sun et al., 2006a, 2006b) and planktonic $\delta^{18}O$ and elemental ratios from the marginal sea sediments (e.g. Wang et al., 2003; Clemens et al., 2008, 2018; Kunkelova et al., 2018), implying that the Northern Hemisphere ice sheet (NHIS) also plays a key role in driving glacial-interglacial monsoon variations.

Climate change in East Asia, including the eastern and southern Asian continent, and the surrounding oceans (e.g. East China Sea, South China Sea, Arabian Sea, Bay of Bengal), is significantly affected by the Asian monsoon circulation (Gao et al., 1962; Ding and Chan, 2005; Wang, 2006), including the East Asian monsoon (EAM) and the Indian summer monsoon (ISM). Over past decades, proxy records from five representative archives (i.e. loess, stalagmite, desert, lake and marine sediments) have been extensively investigated to reconstruct monsoon-induced changes in wind, precipitation, and precipitation isotopes during the Quaternary (e.g. Liu and Ding, 1998; An, 2000; Wang et al., 2005; Wang et al., 2008; An et al., 2011, 2012; Cheng et al., 2016; Chen et al., 2019; Liu et al., 2021). Notably, these proxies exhibit quite different characteristics in terms of trends (weakening vs. strengthening of the monsoon intensity) and rhythms (100- vs. 23-kyr cycles) (e.g. Liu et al., 1999; Sun et al., 2006a; Wang et al., 2008; Wang et al., 2014; An et al., 2015; Cheng et al., 2016), resulting in diverse manifestation of orbital-scale monsoon variability (e.g. Clemens et al., 1991; Ding et al., 1995; An et al., 2011; Wang et al., 2017; Cheng et al., 2021). This, in part, reflects the fact that different proxies record different aspects of monsoonal circulation, including, for example, temperature, wind strength, local precipitation amount, the isotopic composition of precipitation (as a function of source area/transport path dynamics) and/or various combinations thereof. In this review, 'monsoon intensity', unless otherwise stated, generically refers to changes in one or more of these parameters in concert with strengthened circulation.

Dynamically, drivers of orbital-scale climate changes include external forcing of three astronomical parameters (Berger, 1978), internal factors of changing ice-sheets on both hemispheres (Zachos et al., 2001), and atmospheric concentrations of greenhouse gases (Petit et al., 1999). Numerical simulations with general circulation models have long been performed to understand relative impacts of these forcing factors on orbital-scale monsoon variability (e.g. Kutzbach and Otto-Bliesner, 1982; Kutzbach et al., 2008). Sensitivity experiments generally suggest that astronomical parameters, ice sheet, and atmospheric CO_2 concentrations all affect orbital-scale monsoon variability (Prell and Kutzbach, 1987, 1992; Yin et al., 2009; Lu et al., 2013; Liu et al., 2014). Transient simulations reveal that the impacts of insolation, ice and CO_2 on summer precipitation and southerly wind changes since the last glacial maximum are spatially different in the East Asian continent (Liu et al., 2014; Wen et al., 2016). Other simulations show that the specific responses of summer monsoon to ice, CO_2 and astronomical forcing are regionally dependent (Yin et al., 2008, 2009; Araya−Melo et al., 2015; Sun et al., 2019; Lyu et al., 2021). Clearly, different regional responses of the precipitation and wind changes to external and internal forcing can also lead to different conclusions regarding orbital-scale monsoon dynamics (Liu et al., 2014; Cheng et al., 2021).

Proxy-model comparisons, while largely limited to last several climate cycles (e.g. Yin et al., 2008; Shi et al., 2011; Lu et al., 2013; Liu et al., 2014; Sun et al., 2015), have already provided valuable insights into orbital-scale monsoon dynamics. In this review, we extend proxy-data comparison back to the Quaternary by comparing multiple proxy records from five archives in East Asia with the HadCM3 modeling results (i.e. temperature, wind and precipitation). The main objective is to address the spatiotemporal characteristics of Quaternary monsoon change in East Asia and its underlying dynamics. In Section 2, multiple proxy records from loess, cave, lake, and deep-sea sediments are synthesized to reflect changes in ice volume, temperature, wind intensity, and monsoon-induced hydrological and weathering processes. In Section 3, representative proxies are chosen to address the spatiotemporal features of Quaternary climate variations. Evolutionary power spectra of the chosen proxies are then applied to assess the Quaternary evolution of dominant climatic periodicities. In Section 4, simulated changes in temperature, precipitation, and southerly wind are presented to address the spatial expressions of the climate response to astronomical, and ice/CO_2 forcing. Finally, proxies and model results are directly compared to infer the characteristics and dynamics of Quaternary climate changes in the East Asian monsoon-affected region.

2. Archives and proxies

Over the past three decades, more than fifty sites in East Asia and proximal oceans have been studied to address Quaternary climate fluctuations associated with changes in EAM and ISM (Fig. 1, Table 1). Quaternary climate changes in the larger Asian monsoon domain were initially investigated using Chinese loess sequences and marine cores retrieved by the Ocean Drilling Program (ODP) from the Arabian Sea, the Japan Sea, and the South China Sea (e.g. An et al., 1990; Clemens et al., 1991; Tada et al., 1992; Wang et al., 2003). Subsequently, many loess sequences on the Chinese Loess Plateau (CLP) have been studied to reconstruct Quaternary monsoon changes (e.g. An et al., 1990; Chen et al., 1991; Xiao and An, 1999; An, 2000; Ding et al., 2002; Sun et al., 2006a, 2019, 2021; Zhang et al., 2016) (Fig. 1b and Table 1). In addition, eolian-

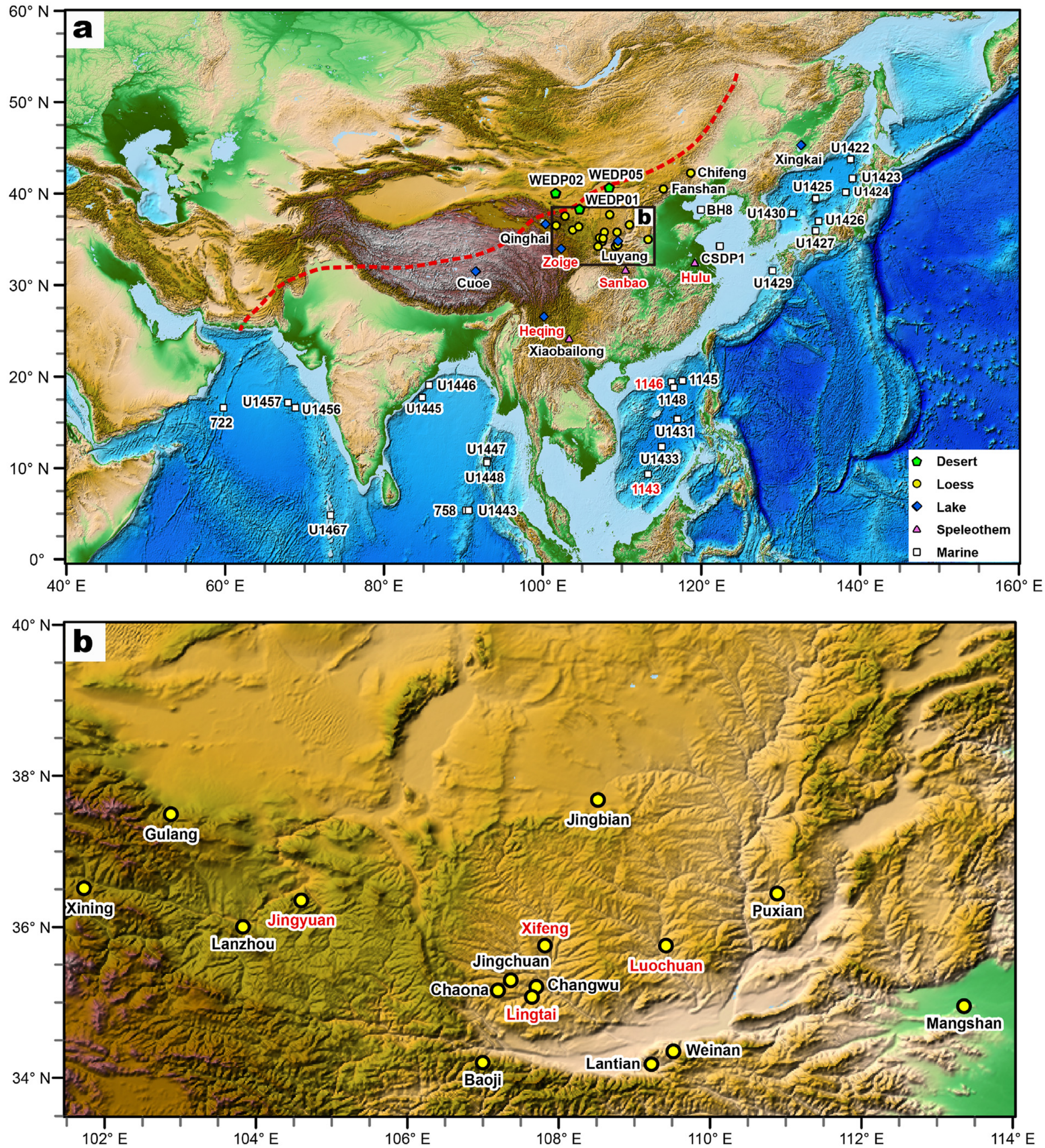

Fig. 1. Location of loess, desert, lake, speleothem, and marine records in East Asia and its surrounding oceans. Dashed line denotes the northern limit of the Asian summer monsoon (Gao et al., 1962; Chen et al., 2019). Detailed information of these sites is presented in Table 1.

lacustrine sediments in northern Chinese deserts (Li et al., 2014b; Wang et al., 2015; Li et al., 2019a; Liu et al., 2021), Lake Qinghai (Fu et al., 2013), and Lake Luyang (Rits et al., 2016) have also been investigated to reflect Quaternary environmental changes associated with East Asian monsoon circulation. Meanwhile, Pleistocene records of ISM changes have been derived from lake sediments from Cuoe (Lü et al., 2001), Heqing (HQ, An et al., 2011), and Zoige Basin (ZB, Zhao et al., 2020).

Sediments in the marginal seas have also been used to reconstruct Quaternary changes in sea level and monsoonal precipitation (e.g. Shi et al., 2016; Liu et al., 2016; Yi et al., 2016). Recent monsoon expeditions conducted by the Integrated Ocean Drilling Program and International Ocean Discovery Program (IODP) have drilled a number of sites in the Japan and East China Seas (e.g. Tada et al., 2018; Irino et al., 2018), South China Sea (e.g. Miao et al., 2017; Gai et al., 2020), Bay of Bengal (Clemens et al., 2016, 2021; France-Lanord et al., 2016), and Arabian Sea (e.g. Betzler et al., 2018; Kunkelova et al., 2018; Pandey et al., 2016). Many proxies from these marine cores have been employed to reflect monsoon-induced changes in chemical weathering, paleoproductivity, detrital influx, and sea surface salinity and temperature (Table 1). Unlike the abundant loess, lake, and marine sediments spanning

Table 1
Lists of Quaternary paleoclimatic records in East Asia and its surrounding oceans.

Archives	Sites	Location	Proxies	Time span (Ma)	References
Loess	Gulang	37.49°N, 102.88°E	Mean, Fe/K	0–1.5	Sun et al. (2021)
	Xining	36.51°N, 101.73°E	MS	0–2	Lu et al. (2012)
	Lanzhou	36.00°N, 103.83°E	Median, MS	0–2.2	Chen et al. (1991); Zhang et al. (2016)
	Jingyuan	36.35°N, 104.60°E	Mean, MS, $\delta^{13}C_{IC}$	0–1.7	Sun et al. (2019)
	Jingbian	37.68°N, 108.52°E	Median, MS	0–3.5	Ding et al. (2005)
	Xifeng	35.75°N, 107.82°E	Quartz Mean, MS	0–7.5	Kukla et al. (1988); Sun et al. (2006a)
	Jingchuan	35.29°N, 107.37°E	Median, MS	0–7.2	Ding et al. (2002)
	Chaona	35.17°N, 107.20°E	>30 μm, MS	0–2.6	Song et al. (2014)
	Changwu	35.20°N, 107.70°E	MS, MS_{FD}, FeD/FeT	0–1.2	Guo et al. (2000)
	Lingtai	35.07°N, 107.65°E	Quartz Mean, MS	0–7.2	Ding et al. (1999); Sun et al. (2006a)
	Luochuan	35.75°N, 109.42°E	Mean, MS	0–2.6	An et al. (1990); Xiao and An (1999); Han et al. (2020)
	Puxian	36.44°N, 110.89°E	Median	0–2.6	Ding et al. (2002)
	Baoji	34.20°N, 107.00°E	Median	0–2.6	Ding et al. (1994, 2002)
	Lantian	34.18°N, 109.23°E	MS, $\delta^{13}C_{IC}$, Rb/Sr	0–5	Zheng et al. (1992); Bloemendal et al. (2018)
	Weinan	34.35°N, 109.52°E	MS	0–2.6	Sun (2005)
	Mangshan	34.95°N, 113.36°E	Median, MS	0–1.1	Jiang et al. (2007); Zheng et al. (2007)
	Fanshan	40.50°N, 115.17°E	Median, MS	0–1.1	Xiong et al. (2001)
	Chifeng	42.31°N, 118.69°E	MS	0–1.2	Zeng et al. (2016)
Desert	WEDP01	38.37°N, 104.65°E	MS, Grain size, Magnetic parameters	0–3.55	Li et al. (2014b); Liu et al. (2021)
	WEDP02	40.01°N, 101.73°E	Grain size, a* CaCO3 content	0–1.2	Wang et al. (2015)
	WEDP05	40.75°N, 108.39°E	Mean, TOC,C/N	0–1.7	Li et al. (2019a)
Speleothem	Hulu	32.50°N, 119.17°E	$\delta^{18}O$	0–0.075	Wang et al. (2001)
	Sanbao	31.67°N, 110.43°E	$\delta^{18}O$	0–0.64	Wang et al. (2008); Cheng et al. (2016)
	Xiaobailong	24.20°N, 103.35°E	$\delta^{18}O$	0–0.25	Cai et al. (2015)
Lake	Xingkai	45.31°N, 132.58°E	Pollen	0–3.6	Xin et al. (2019)
	Cuoe	31.52°N, 91.55°E	Pollen, Median, Rb/Sr	0–2.8	Lü et al. (2001); Shen et al. (2004)
	Qinghai	36.67°N, 100.38°E	Mean	0–5.1	Fu et al. (2013)
	Zoige	33.97°N, 102.33°E	Arboreal pollen	0–1.7	Zhao et al. (2020)
	Luyang	34.82°N, 109.53°E	Median, $CaCO_3$	0–1.1	Rits et al. (2016)
	Heqing	26.57°N, 100.17°E	*Tsuga*, ISM index	0–2.6	An et al. (2011)
Marginal Seas	BH8	38.28°N, 119.99°E	a*, b*, S/Cl	0–1.06	Shi et al. (2016)
	CSDP1	34.30°N, 122.37°E	M_{rs}/MS	0–3.5	Liu et al. (2016)
	U1429	31.62°N, 129.00°E	$\delta^{18}O_b$, $\delta^{18}O_p$, MS, L*, a*, b*	0–0.04	Tada et al. (2015); Clemens et al. (2018)
Japan Sea	U1422	43.77°N, 138.83°E	K, MS, L*, a*, b*	0–3.9	Tada et al. (2015); Zhang et al. (2018b)
	U1423	41.70°N, 139.08°E	MS, L*, a*, b*	0–5	Tada et al. (2015); Irino et al. (2018)
	U1424	40.19°N, 138.23°E	MS, L*, a*, b*	0–4	Tada et al. (2015, 2018)
	U1425	39.50°N, 134.45°E	MS, L*, a*, b*	0–10	Tada et al. (2015)
	U1426	37.03°N, 134.80°E	MS, L*, a*, b*	0–5	Tada et al. (2015)
	U1427	35.97°N, 134.43°E	MS, L*, a*, b*	0–1.4	Tada et al. (2015)
	U1430	37.90°N, 131.54°E	MS, L*, a*, b*	0–15	Tada et al. (2015)
South China Sea	1143	9.36°N, 113.29°E	$\delta^{18}O_b$, SST, Ti/Al, Hm/Gt	0–5	Tian et al. (2002), 2011; Zhang et al. (2009); Li et al. (2011)
	1145	19.58°N, 117.63°E	$\delta^{18}O_p$, MS, L*, a*, b*	0–3.5	Wang et al. (2000, 2003); Boulay et al. (2005)
	1146	19.45°N, 116.27°E	$\delta^{18}O_b$, $\delta^{18}O_p$, SST, Ba/Al	0–5	Clemens et al. (2008); Herbert et al. (2010)
	1148	18.84°N, 116.57°E	$\delta^{18}O_p$	0–6	Wang et al. (2003); Jian et al. (2001)
	U1431	15.38°N, 117.00°E	MS, Hm/Gt	0–6.5	Gai et al. (2020)
	U1433	12.37°N, 115.05°E	Fungal spore	0–17	Miao et al. (2017)
Bay of Bengal	758	5.38°N, 90.35°E	$\delta^{18}O_b$, $\delta^{18}O_p$	0–7	Farrell and Janecek (1991); Chen et al. (1995)
	U1443	5.38°N, 90.36°E	MS, L*, a*, b*	0–3.4	Clemens et al. (2016)
	U1445	17.75°N, 84.83°E	TOC, $CaCO_3$, C/N	0–2.3	Lee et al. (2020)
	U1446	19.08°N, 85.73°E	$\delta^{18}O_b$, $\delta^{18}O_p$, SST, Rb/Ca	0–1.5	Clemens et al. (2021)
	U1447	10.80°N, 93.00°E	MS, L*, a*, b*	0–10	Clemens et al. (2016)
	U1448	10.63°N, 93.00°E	MS, L*, a*, b*	0–7	Clemens et al. (2016)
Ariabian Sea	722	16.62°N, 59.80°E	$\delta^{18}O_b$, $\delta^{18}O_p$, SST,	0–3.5	Clemens et al. (1996); Herbert et al. (2010)
	U1456	16.62°N, 68.84°E	MS, L*	0–10	Pandey et al. (2016)
	U1457	17.17°N, 67.93°E	MS, L*	0–10	Pandey et al. (2016)
	U1467	4.85°N, 73.28°E	Fe/K, Ca/K	0–2	Betzler et al. (2018); Kunkelova et al. (2018)

MS-magnetic susceptibility; $\delta^{13}C_{IC}$-$\delta^{13}C$ of loess carbonate; TOC-Total Organic Carbon; ISM index-Indian summer monsoon index; M_{rs}/MS-ratios of saturation remanence (M_{rs}) to magnetic susceptibility; SST-Sea surface temperature; MS_{FD}-frequency dependent magnetic susceptibility; FeD/FeT-ratios of extractable free Fe_2O_3 to total Fe_2O_3; Hm/Gt-Hematite/Goethite ratio; $\delta^{18}O_b$-$\delta^{18}O$ of benthic foraminifera; $\delta^{18}O_p$-$\delta^{18}O$ of planktonic foraminifera.

the Quaternary, absolutely dated speleothem records mainly span the last 640 ka (e.g. Wang et al., 2008; Cai et al., 2015; Cheng et al., 2009; 2016).

The Asian monsoon is driven by the land-ocean thermal gradient and cross-equatorial pressure gradient over the Asian-Indian-Pacific region (Webster et al., 1998; Ding and Chan, 2005; Wang and Ding, 2008; Geen et al., 2020). The geographic location of the East Asian continent and its surrounding oceans conveniently allows for a detailed land-ocean comparison and further exploration of the dynamics and characteristics of Quaternary monsoon change. Here four loess sequences (JY-Jingyuan, LC-Luochuan, XF-Xifeng, and LT-Lingtai) and two marine records (ODP sites 1143 and 1146) are chosen to assess Quaternary EAM change, and two lake records (Zoige, and Heqing) are selected to infer ISM variability (see red labels in Fig. 1). These records were chosen for their long duration (>1.5 Ma), millennial resolution (<4 kyr), well constrained age models, and availability of multiple proxies sensitive to orbital-scale monsoon change. In addition, speleothem $\delta^{18}O$ records in East Asia have also been employed to assess orbital-scale monsoon changes over the last 640 kyr (Wang et al., 2001, 2008; Cai et al., 2015; Cheng et al., 2016).

2.1. Loess sequences

Chinese loess has been investigated as a unique continental archive to reconstruct glacial-interglacial fluctuations of the East Asian monsoon since the 1990s (e.g. An et al., 1990; Ding et al., 1995; Liu and Ding, 1998; An, 2000; Maher, 2016). Three classic loess profiles in the central CLP and one high-sedimentation-rate loess sequence from the northwestern CLP are selected for addressing orbital-scale fluctuations of the East Asian monsoon during the Quaternary. Grain size parameters (e.g. mean, median, and coarse fraction) of loess deposits have been widely employed to reflect the strength of dust transport dynamics (i.e. coarser grain-size reflecting stronger winter monsoon) (An et al., 1991a; Xiao et al., 1992; Ding et al., 2002; Lu et al., 2004; Sun et al., 2006a; Hao et al., 2012). Mean grain-size results of three loess-paleosol sequences on the central CLP exhibit significant glacial-interglacial fluctuations spanning the last 2.6 Ma (Fig. 2a and b, Sun et al., 2006a; Han et al., 2020). By contrast, JY loess sequence from the northwestern CLP usually exhibits much stronger glacial-interglacial variation and persistent millennial-scale oscillations, as it's proximal to the northern Chinese deserts (Fig. 2c, Sun et al., 2019).

Magnetic susceptibility (MS) has been widely used to infer the summer monsoon intensity since strong pedogenesis leads to enhanced formation of secondary magnetic minerals (Zhou et al., 1990; An et al., 1991b; Maher and Thompson, 1995). MS records from the central CLP exhibit large amplitude fluctuations (e.g. An et al., 1990; Xiao and An, 1999; Lu et al., 1999; Sun et al., 2006a), corresponding well to the glacial-interglacial alternations between loess and paleosol layers (Fig. 2c and d). In contrast, MS variation at JY profile is only sensitive to interglacial climate changes and exhibits precession-scale variations during the last three interglacials (Fig. 2f, Sun et al., 2019). In addition to the widely employed MS proxy, the $\delta^{13}C$ records of inorganic carbonate in loess sediments have been proven as sensitive proxies for precipitation-induced vegetation change (Liu et al., 2011; Yang et al., 2015). A 1.7-Myr $\delta^{13}C$ record of loess carbonate at JY section exhibits a different cyclic shift from a dominant 23-kyr cycle before 1.2 Ma to combined periodicities on 100, 41, and 23-kyr bands (Fig. 2g, Sun et al., 2019). Unlike evident glacial-interglacial cycles revealed by loess grain size and magnetic susceptibility records, the Sr/Ca ratio of microcodium in Chinese loess (a novel proxy for precipitation)

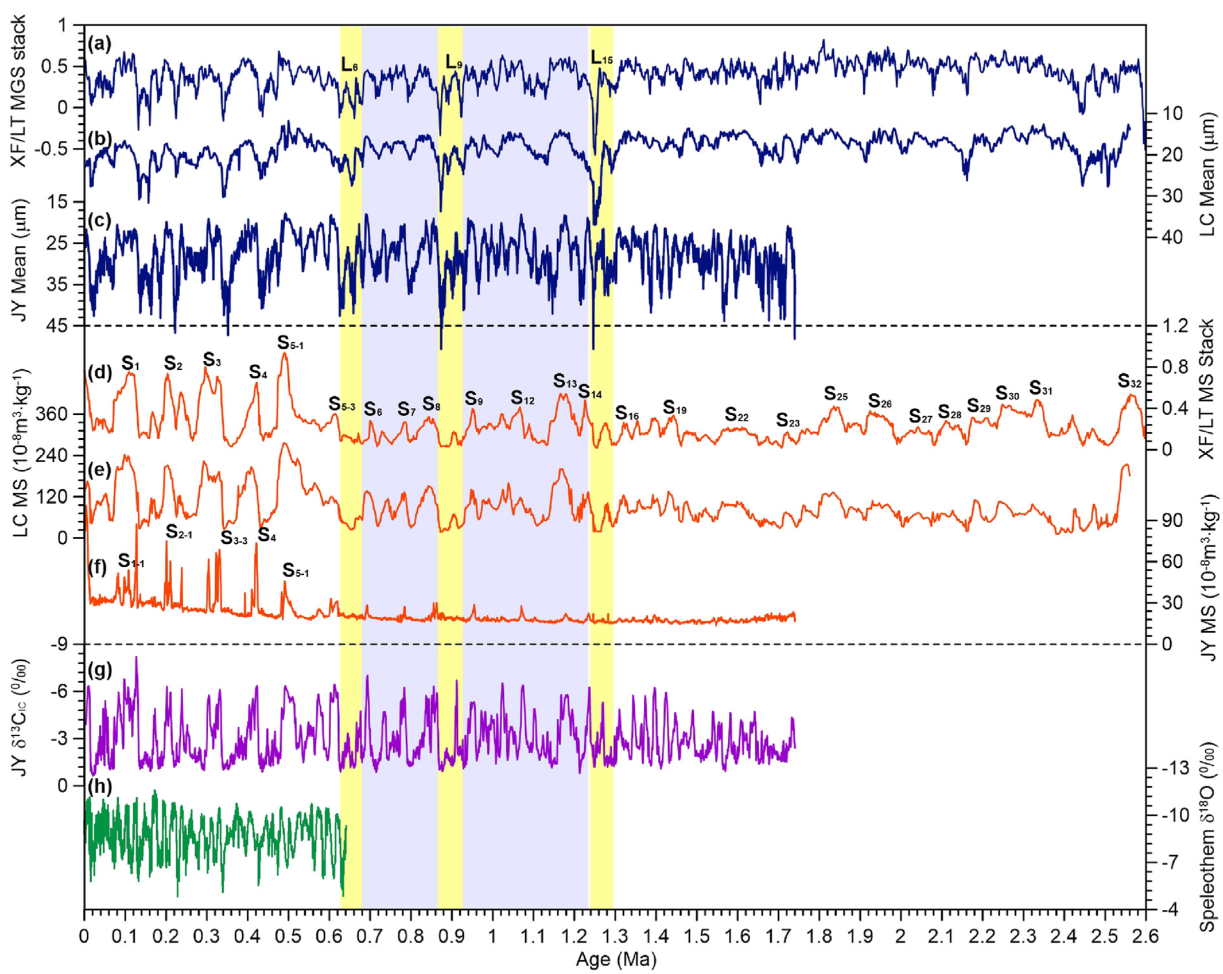

Fig. 2. Comparison of loess proxies with speleothem $\delta^{18}O$ record. From top to bottom: (a) Quartz mean grain-size stack (MGS) of Xifeng/Lingtai (XF/LT, Sun et al., 2006a), (b) Mean grain size of Luochuan (LC, Han et al., 2020), (c) Mean grain size of Jingyuan (JY, Sun et al., 2019), (d) Magnetic susceptibility (MS) stack of XF/LT (Sun et al., 2006a), (e) MS of LC (Han et al., 2020), (f) MS of JY (Sun et al., 2019), (g) $\delta^{13}C_{IC}$ of JY (Sun et al., 2019), and (h) speleothem $\delta^{18}O$ records of Hulu/Sanbao caves (Wang et al., 2001, 2008; Cheng et al., 2016). Light blue bar denotes the Mid-Pleistocene transition, and three yellow bars indicate loess marker layers of L_6, L_9, and L_{15}. (For interpretation of the references to colour in this figure legend, the reader is referred to the Web version of this article.)

demonstrates persistent obliquity cycles through the Pleistocene (Li and Li, 2014; Li et al., 2016).

2.2. Lake sediments

Lake sediments are valuable for providing hydrological and weathering records of the lake catchments, which are greatly influenced by both regional and global climate changes (Williams et al., 2001; An et al., 2011). Two lake records from the Heqing (HQ) (An et al., 2011) and Zoige Basin (ZB, Zhao et al., 2020) are selected to address orbital-scale ISM change. Paleolake HQ located in southwestern China is greatly influenced by the ISM change, characterized by warm wet summer and cool dry winter (Shen et al., 2007; An et al., 2011). *Tsuga* flourishes under moderately warm and humid conditions and therefore higher *Tsuga* contents correspond to warmer interglacial periods in Heqing record (Fig. 3a). The total organic carbon (TOC) content in the lacustrine sediments is closely correlated to ISM-induced changes in catchment biomass and lake productivity, capturing the strong monsoon events during interglacials (Fig. 3b). The Rb/Sr ratio reflects the weathering intensity within the catchment area, sensitive to weak monsoon events during glacial times (Fig. 3c). Thus, Rb/Sr and TOC from paleolake HQ were stacked as an ISM index to reflect full amplitude of glacial-interglacial ISM variability (Fig. 3d). The Zoige Basin (ZB) located on the eastern Tibetan Plateau is also affected by the ISM climate (Zhao et al., 2020). In this region, the density and elevation limits of forests are mainly controlled by temperature rather than precipitation, since the moisture availability is plentiful for plant growth (Shen et al., 2005). Therefore, the arboreal pollen abundance from the ZB sediment is regarded as a primary reflection of temperature change (AP%, Fig. 3e).

2.3. Deep-sea sediments

After two monsoon-focused ODP expeditions in the Arabian Sea and South China Sea (e.g. de Menocal et al., 1991; Clemens et al., 1991; Wang et al., 2000, 2003), additional marine cores have been recently retrieved from the Japan Sea, East China Sea, South China Sea, Bay of Bengal, and Arabian Sea in the IODP monsoon-related expeditions (Fig. 1 and Table 1, e.g. Clemens et al., 2016; Pandey et al., 2016; Tada et al., 2015, 2018; Betzler et al., 2018). Yet long, high-resolution and multiple proxies sensitive to monsoon changes from these sites are still limited (e.g. Kunkelova et al., 2018; Irino et al., 2018; Clemens et al., 2021). Here we select proxy records of ODP sites 1143 and 1146 in the South China Sea to address their sensitivity to EAM changes. These marine-based proxies can be divided into three types: $\delta^{18}O$ of benthic ($\delta^{18}O_b$) and planktonic ($\delta^{18}O_p$) foraminifera, sea surface temperature (SST), and mineral and chemical indicators. $\delta^{18}O_b$ record has long been regarded as a proxy for changes in global ice volume and deep-water temperature (Shackleton, 2000; Zachos et al., 2001; Elderfield et al., 2012). Comparably, $\delta^{18}O_p$ is regarded as a function of sea surface/subsurface temperature, sea level and local salinity (Bemis et al., 1998; Elderfield and Ganssen, 2000; Rohling, 2007). Removal of the temperature and global sea-level effects from $\delta^{18}O_p$ can isolate the sea surface salinity component, which is usually employed to reflect rainfall/runoff change in monsoon-affected area (e.g. the Yangtze River Valley, Clemens et al., 2018). The benthic $\delta^{18}O$ records of ODP sites 1143 and 1146 demonstrate quite similar glacial-interglacial fluctuations (Fig. 4a and b). $\delta^{18}O_p$ data obtained from *Globigerinoides* (*G. ruber* and *G. sacculifer*) of ODP site 1143 site also exhibit similar glacial-interglacial variability (Fig. 4c).

SST changes can be inferred from alkenone U^{K}_{37}' index, Mg/Ca ratios, and foraminifera transfer functions. The unsaturation index of alkenones (U^{K}_{37}') produced by coccolithophores is sensitive to the mean annual SST (Müller et al., 1998). Two alkenone-based time series from ODP sites 1143 and 1146 display significant glacial-interglacial SST changes through the Quaternary (Fig. 4d and e, Herbert et al., 2010; Li et al., 2011). Mineral and elemental proxies have been used to reconstruct the evolution of the Asian monsoon-induced productivity and chemical weathering in source regions (e.g. Clemens et al., 2008; Zhang et al., 2009; Tian et al., 2011). Since hematite formation is favored by dry conditions whereas goethite is formed under relatively humid conditions (Zhang et al., 2009), the

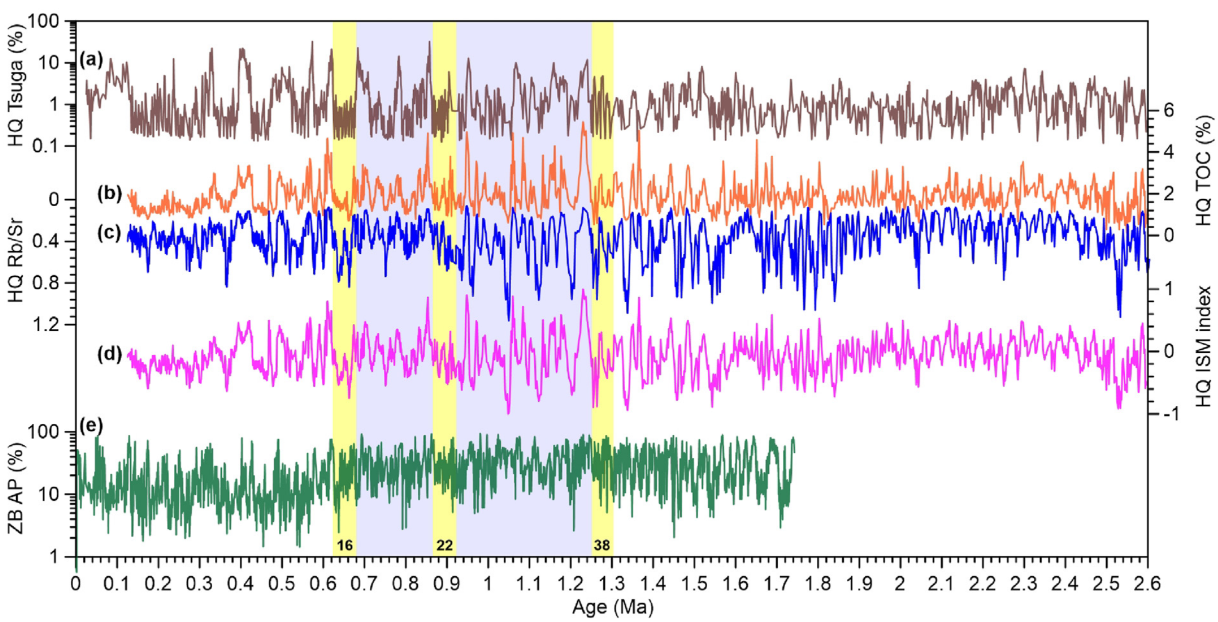

Fig. 3. Variations of proxy indicators from Heqing (HQ) and Zoige Basin (ZB). (a–d) *Tsuga* content, TOC, Rb/Sr ratio, and ISM index of HQ paleolake sediments (An et al., 2011); (e) Arboreal pollen abundance (AP%) of ZB sediments (Zhao et al., 2020). Light blue bar denotes the Mid-Pleistocene transition, and three yellow bars indicate three extreme glaciations that correspond to marine isotope stages (MIS) 16, 22, and 38. (For interpretation of the references to colour in this figure legend, the reader is referred to the Web version of this article.)

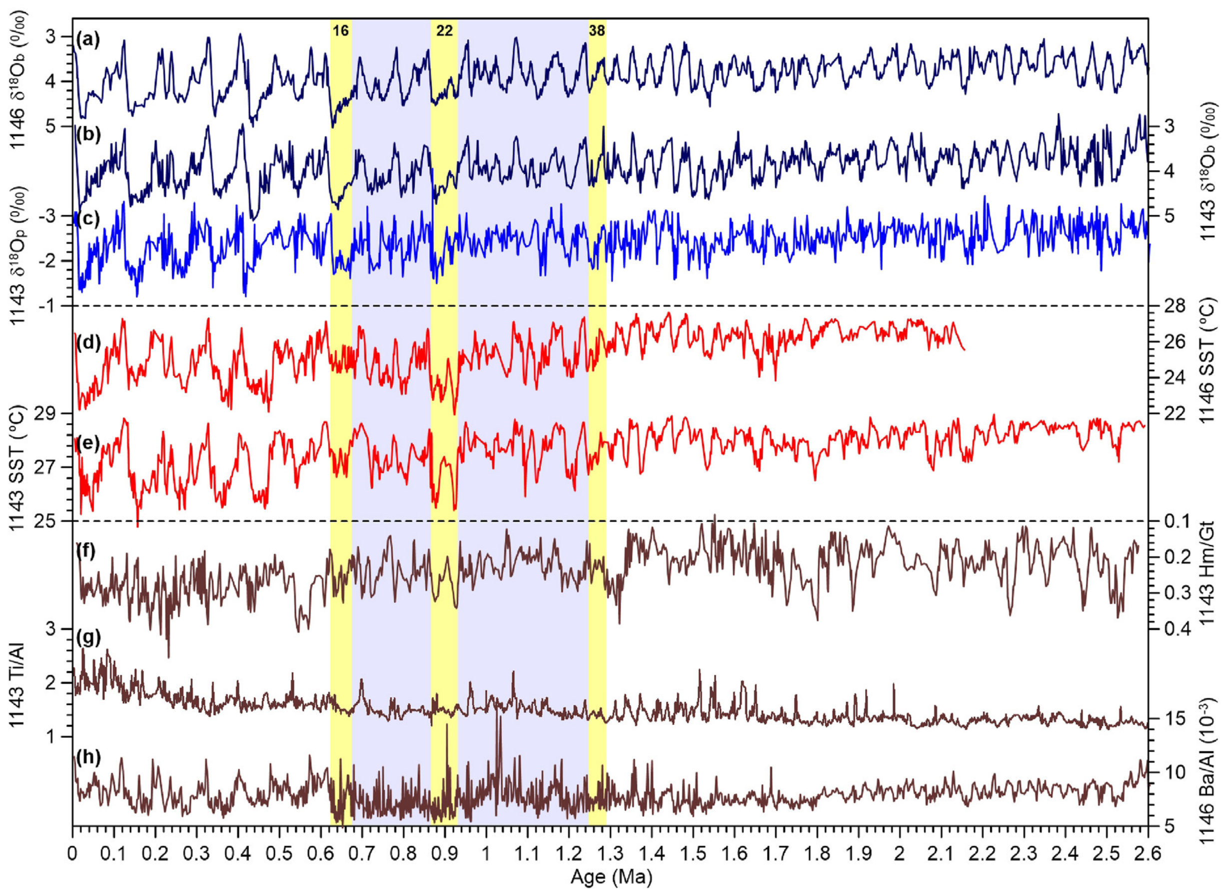

Fig. 4. Proxy records of ODP sites 1143 and 1146 from the South China Sea. From top to bottom: (a, b) Benthic $\delta^{18}O$ of ODP sites 1143 (Tian et al., 2002) and 1146 (Clemens et al., 2008), (c) Planktonic $\delta^{18}O$ of ODP site 1143 (Tian et al., 2002), (d, e) Alkenone-based SST records of ODP sites 1146 (Herbert et al., 2010) and 1143 (Li et al., 2011), (f) Hematite/Goethite (Hm/Gt) ratio of ODP site 1143 (Zhang et al., 2009), (g) Ti/Al ratio of ODP site 1143 (Tian et al., 2011), and (h) Ba/Al ratio of ODP site 1146 (Clemens et al., 2008). Light blue bar denotes the Mid-Pleistocene transition, and three yellow bars indicate extreme glaciations during marine isotope stages (MIS) 16, 22, and 38. (For interpretation of the references to colour in this figure legend, the reader is referred to the Web version of this article.)

hematite/goethite (Hm/Gt) ratio at ODP site 1143 is precipitation-dependent and highly sensitive to summer monsoon change (Fig. 4f). The Ti/Al is interpreted as an indicator of monsoon-induced weathering intensity (Fig. 4g), since Ti is more conservative than Al during chemical weathering processes (Wehausen and Brumsack, 2002; Wei et al., 2006; Tian et al., 2011). Meanwhile, the Ba/Al ratio is often used to infer the monsoon-induced paleoproductivity (Fig. 4h), because increased Ba flux is associated with the enhanced nutrient supply owing to strong winter monsoon (Wehausen and Brumsack, 2002; Clemens et al., 2008).

3. Characteristics of Quaternary climate change

3.1. EAM evolution inferred by loess proxies

Proxy records from Chinese loess deposits can well reflect monsoonal wind and precipitation changes (An et al., 1990; Liu and Ding, 1998; Xiao and An, 1999; An, 2000; Ding et al., 2002; Lu et al., 2004; Sun et al., 2010). East Asian winter monsoon variation, mainly inferred by loess grain-size parameters, exhibit large amplitude fluctuations at glacial-interglacial time scales (e.g. Ding et al., 1995, 2002; Xiao and An, 1999; Sun et al., 2006a). Grain-size results of loess deposits assembled herein exhibit a coarsening trend from the early to the mid-late Pleistocene (Fig. 2a–c). Remarkable coarsening of two thick silt loess units (L_9 and L_{15}) is evident in Chinese loess sequences, likely related to regional tectonic activities of the northern Tibetan Plateau and/or stepwise evolution of the Yellow River (Xiao and An, 1999; Sun and Liu, 2000a; Li et al., 2014a; Han et al., 2012). The amplitude and duration of glacial-interglacial fluctuations of loess grain-size increased significantly during 1.2–0.9 Ma, reflecting the gradual expansion of the NHIS across the MPT (Lisiecki and Raymo, 2005; Clark et al., 2006). Besides sharing similar glacial-interglacial fluctuation, mean grain-size of high-sedimentation-rate loess sequence from the northwestern CLP are characterized by more distinctive precession- and millennial-scale oscillations (Fig. 2c, Sun et al., 2019).

The MS variations of three loess sequences from the central CLP exhibit similar glacial-interglacial fluctuations, superimposed by two stepwise increases at palaeosols S_{14} (~1.25 Ma) and S_5 (~0.5 Ma) (Fig. 2d and e). However, the MS record at JY profile exhibits a significant strengthening of the summer monsoon intensity in S_4 (Fig. 2f), consistent with the Mid-Brunhes event occurred at the marine isotope stage (MIS) 12/11 boundary (Jansen et al., 1986; Lisiecki and Raymo, 2005; Berger et al., 2016). Due to relatively high sedimentation rates of loess deposits in the western CLP (Sun et al., 2006b, 2019), MS variations of three paleosol layers (S_1–S_3) exhibit three peaks corresponding to precession-driven insolation cycles. MS records of loess layers in the western CLP are less sensitive to summer monsoon changes since the precipitation is relatively low during glacial periods (Chen et al., 1991; Sun et al., 2006b; Lu et al., 2012; Maher, 2016). By contrast, the carbon isotope of loess carbonates in the northwestern CLP is very sensitive to monsoon-induced vegetation changes (Liu et al., 2011; Sun et al., 2015). A 1.7-Myr $\delta^{13}C$ record of inorganic carbonate ($\delta^{13}C_{IC}$) from JY section exhibits a unique periodicity transition from dominant 21-kyr before 1.2 Ma to combined 100- and 21-kyr cycles after 0.7 Ma (Fig. 2g, Sun et al., 2019).

Variations of loess grain-size and MS suggest that the amplitudes of the East Asian monsoon increased remarkably after 1.25 Ma, as manifested by simultaneous enhancing of the summer monsoon intensity during interglacials and the winter monsoon strength during glacial periods (Ding et al., 2002; Sun et al., 2006a). Similar long-term trend and cycle-by-cycle correlation of loess grain-size and benthic $\delta^{18}O$ suggest that Quaternary winter monsoon evolution is driven by the waxing and waning of the NHIS (Ding et al., 1995; Liu et al., 1999). However, the MS records values increased remarkably in S_{14} and S_{5-1} (Fig. 2d and e), implying that stepwise strengthening of the summer monsoon during the Quaternary was likely related to the phased uplift of the northeastern Tibetan Plateau around 1.2–0.9 Ma (Sun and Liu, 2000a; Li et al., 2014a) and/or the asymmetric developments of bi-polar and Eurasian ice sheets around 0.5 Ma (Yin et al., 2008, 2009; Guo et al., 2009). Unlike the marked MS increase in S_{5-1} to S_4 (Ding et al., 2002; Sun et al., 2006b, 2021; Ao et al., 2020), the loess $\delta^{13}C_{IC}$ and speleothem $\delta^{18}O$ records exhibit a uniform amplitude during the Mid-Brunhes epoch (Fig. 2g and h, Cheng et al., 2016; Sun et al., 2019). Such a discrepancy indicates that prolonged pedogenesis duration of paleosol layers and increased detrital input of magnetic minerals might also affect the enhancing of magnetic susceptibility in Chinese loess (Maher and Thompson, 1995; Sun and Liu, 2000b). Moreover, since the upper and middle reaches of the Yellow River as potential sources of loess deposit have been expanded stepwise during the Quaternary (Nie et al., 2015), provenance shift may potentially complicate interpretation of the mineral and geochemical proxy indicators from loess deposits (Zhang et al., 2021).

3.2. ISM variability inferred by lake sediments

The pollen and geochemical records from the sediments of paleolake HQ are presented to infer the ISM variability over the past 2.6 Ma. High-amplitude fluctuation in *Tsuga* content varies at glacial-interglacial time scales (Fig. 3a), implying that the temperature variation in the Heqing basin is coupled with change in the NHIS (An et al., 2011). Rb/Sr minima and TOC maxima reflect an enhanced ISM associated with interglacial ice minima, while the glacial ISM intensity can be well inferred from the TOC minima and Rb/Sr maxima (Fig. 3b and c). Amplitude of the ISM variability is relatively large during 1.8–0.9 Ma, compared with those in the other two time intervals (Fig. 3d). Varying amplitudes of the ISM variability through the Quaternary are attributed to different roles of the NHIS and the Antarctica temperature in driving glacial-interglacial ISM variability. During 1.8–0.9 Ma, the ISM was dominantly affected by the thermal pull of the NHIS, whereas before 1.8 Ma and after 0.9 Ma the pressure push caused by the Antarctica temperature change could offset the thermal pull effect, resulting in decreased amplitude of the glacial-interglacial ISM variability (An et al., 2011).

In the Zoige Basin, vegetation density is greatly influenced by the ISM intensity, and the AP% likely reflects temperature-induced changes in the density and elevation limit of the forest (Zhao et al., 2020). The AP% and other pollen records from the ZB reveal two major transitions of the vegetation and climate changes around 1.5 and 0.6 Ma, respectively (Fig. 3e). The latter transition is characterized by a significant shift from high-frequency oscillations of the AP% before 0.6 Ma to low-frequency fluctuations afterwards. The long-term cooling trend and two remarkable transitions reveal that the dominant factor driving vegetation change in the Zoige Basin shifted from low-latitude insolation before 1.5 Ma to high-latitude ice volume after 0.6 Ma. Notably, ZB AP reveals a relative cooling trend during glacials after 0.6 Ma, in contrast to the HQ *Tsuga* content that suggests a warming trend during interglacials after 0.8 Ma. Such a discrepancy is likely attributed to different sensitivities of these pollen indicators to regional changes in temperature, precipitation, and vegetation.

3.3. EAM imprints in the South China Sea sediments

$\delta^{18}O_b$ records of two ODP sites from the South China Sea share identical glacial-interglacial fluctuations over the past 2.6 Ma (Fig. 4a and b, Tian et al., 2002; Clemens et al., 2008). Sawtooth-shaped variations and a gradual long-term cooling trend are evident after the MPT, suggesting globally simultaneous changes in ice volume and oceanic temperature. Extreme glaciations occurred after 0.7 Ma, corresponding to marine isotope stage (MIS) 16, followed by large-amplitude glacial-interglacial fluctuations. While planktonic foraminifera have experienced strong regional and seasonal fluctuations in temperature and freshwater balance, the saw-tooth pattern of the glacial-interglacial cycles is also evident in the post-MPT planktonic $\delta^{18}O$ record from the ODP site 1143 (Fig. 4c). The Alkenone-based SST records in the South China Sea are characterized by a long-term cooling trend since ~2.6 Ma and an abrupt decrease around 0.9 Ma (Fig. 4d and e, Herbert et al., 2010; Li et al., 2011). While general cooling trends are well recognized in the $\delta^{18}O_b$, $\delta^{18}O_p$, and SST records, the timing and amplitude of glacial extremes are dissimilar among these three proxies. Both $\delta^{18}O_p$ and SST variations reveal that extreme cooling first occurred during MIS 22, likely related to an abrupt increase in the Antarctic ice volume (Elderfield et al., 2012). Extreme glaciation inferred by benthic $\delta^{18}O$ occurred around 0.65 Ma, lagging the other two records by ~0.25 Myr, implying that significant expansion of the NHIS and increased ice-rafted debris in the North Atlantic likely occurred at the end of the MPT (Hodell et al., 2008; Naafs et al., 2013). Overall, these three proxies mostly reflect global climate signals, rather than the EAM imprints.

Elemental and mineral proxies from the South China Sea sediments provide valuable insights into monsoon-related changes in oceanic productivity and continental weathering (Fig. 4f–h). The Ba/Al ratio of ODP site 1146, as an indicator of monsoon-driven paleoproductivity change, displayed a long-term decreasing trend between 2.6 and 1.2 Ma and relatively large amplitude fluctuations afterwards (Clemens et al., 2008). In contrast, the Ti/Al ratio at ODP site 1143, as an indicator of monsoon-induced weathering intensity was enhanced remarkably around 1.6 Ma and continuously strengthened since 0.6 Ma (Tian et al., 2011), consistent with the long-term trend inferred by the mineralogical ratio of chlorite/(chlorite + hematite + goethite) (Clift et al., 2008). Unlike the generally increasing of the Ti/Al ratio, the Hm/Gt ratio from ODP Site 1143 is characterized by a gradual weakening of the summer monsoon intensity, superimposed by two stepwise shifts around 1.25 and 0.55 Ma (Zhang et al., 2007, 2009; Ao et al., 2011). Compared with the loess, lake, and speleothem proxies, these mineral and elemental indicators from the South China Sea exhibit different variation patterns in terms of both long-term trend and glacial-interglacial amplitude through the Quaternary, implying complicated impacts of the EAM variations recorded in the South China Sea sediments (Wang et al., 2005).

3.4. Periodicities of Quaternary climate change

To assess the evolution of climatic periodicity during the Quaternary, evolutionary power spectral analyses were performed on representative proxy records using the Acycle software of Li et al. (2019b). Evolutionary power spectra of six representative proxies from loess and lake archives are presented to address periodic evolution of the EAM and ISM changes on land (Fig. 5). Mean grain-size stack (MGS) from XF/LT loess sections is characterized by an onset of a weak 100-kyr cycle at ~1.2 Ma, followed by strong 100-kyr cycles after ~0.7 Ma (Sun et al., 2006a). Obliquity cycle is relatively stronger before 0.7 Ma than afterwards due to the growing influence of the 100-kyr ice-age cycles, while the precession cycles are very weak and discontinuously present through the Quaternary (Fig. 5a). Similar periodic transition during the MPT was also found in other grain-size (Liu et al., 1999; Ding et al., 2002) and MS time series (Heslop et al., 2002; Lu et al., 2004). Over the past 2.6 Ma, relative intensities of spectral peaks at three orbital periods slightly differ between MGS and MS time series. Besides the strong 41-kyr cycles, the MGS spectrum displays relatively weak 100-kyr cycle and distinct 23- and 19-kyr peaks, differing from the persistent strong 100-kyr peak and insignificant precession cycle in the MS spectrum (Fig. 5b). Unlike loess proxies from the central CLP, the evolutionary spectrum of JY $\delta^{13}C_{IC}$ record shows a different transition from a dominant 23-kyr cycle prior to 1.2 Ma, to combined 100-, 41-, and 23-kyr cycles afterwards (Fig. 5c).

For two lake records, evolutionary power spectra of three proxies exhibit different characteristics at three orbital periods. The spectrum of the HQ ISM index exhibits a combined pattern of three orbital periods before 1.8 Ma and after 0.9 Ma, and a dominant 41-kyr cycle between 1.8 and 0.9 Ma (Fig. 5e). Besides three orbital periods in the ISM index, the spectrum of HQ *Tsuga* content reveals more orbital harmonic periodicities (Fig. 5d). This evolution pattern is consistent with different roles of the NHIS and the Antarctica temperature in driving the ISM variability. Unlike the complex spectra of HQ proxies, the AP% spectrum exhibits a persistent 41-kyr cycle through the last 1.7 Myr, as well as a strong 19-kyr cycle until 0.6 Ma and a clear 100-kyr cycle after 0.6 Ma (Fig. 5f). The spectral results of these loess- and lake-derived proxies confirm diverse expression of Quaternary monsoon changes on the land.

Evolutionary power spectra of five proxy indicators from ODP site 1143 and the Ba/Al ratio of ODP site 1146 also exhibit different evolving periodicities of monsoon-related changes in the South China Sea and South Asian continent (Fig. 6). Similar to the global benthic $\delta^{18}O$ stack (Lisiecki and Raymo, 2005), $\delta^{18}O_b$ spectrum shows an evident MPT from 41-kyr to 100-kyr cycles around 1.2 Ma, consistent with the spectra of SST, Ba/Al, and XF/LT MGS records. In contrast, $\delta^{18}O_p$ spectrum exhibits a mixed pattern of 100-, 41-, 23/19-kyr periods before 1.8 Ma, quite similar to those of the Ti/Al, Hm/Gt ratios, and the HQ ISM records. Since 1.8 Ma, the $\delta^{18}O_p$ spectrum also displays a transition from 41 to 100 kyr cycles around 1.2 Ma, whereas both 41- and 100-kyr cycles are persistently present in the other two proxies. Notably, evolutionary spectra of the Ti/Al and Hm/Gt ratios show all orbital peaks at 100, 41, 23, and 19-kyr bands, and no clear transition in periodicity is found across the MPT. Since the 23- and 19-kyr cycles are discontinuously presented in the spectra of the Ti/Al and Hm/Gt ratios, implying a distinct impact of insolation on the chemical weathering in the terrestrial source areas of Southern Asia. Moreover, presence of the 100-kyr cycles in most of these proxies (i.e. loess MS, HQ ISM, $\delta^{18}Op$, SST, Ba/Al, Ti/Al, and Hm/Gt), particularly during the early Pleistocene, confirms that eccentricity likely plays a key role in modulating low-latitude climatic changes (Clemens and Tiedemann, 1997).

Based on the relative weights and evolution of power in the three orbital components (Figs. 5 and 6), we tentatively characterize the proxy records into four types. Type 1 (loess MGS and MS, $\delta^{18}O_b$, SST, and Ba/Al ratio) is characterized by the conventional MPT transition from 41- to 100-kyr cycles between 1.2 and 0.7 Ma, which are strongly coupled with the NHIS change. Type 2 (ZB AP%, HQ ISM and *Tsuga* content, and ODP1143 $\delta^{18}O_p$) displays a shift from mixed 41- and 23-kyr cyclicities to a combination of 100-, 41- and 23-kyr cycles, implying that combined effects of astronomical

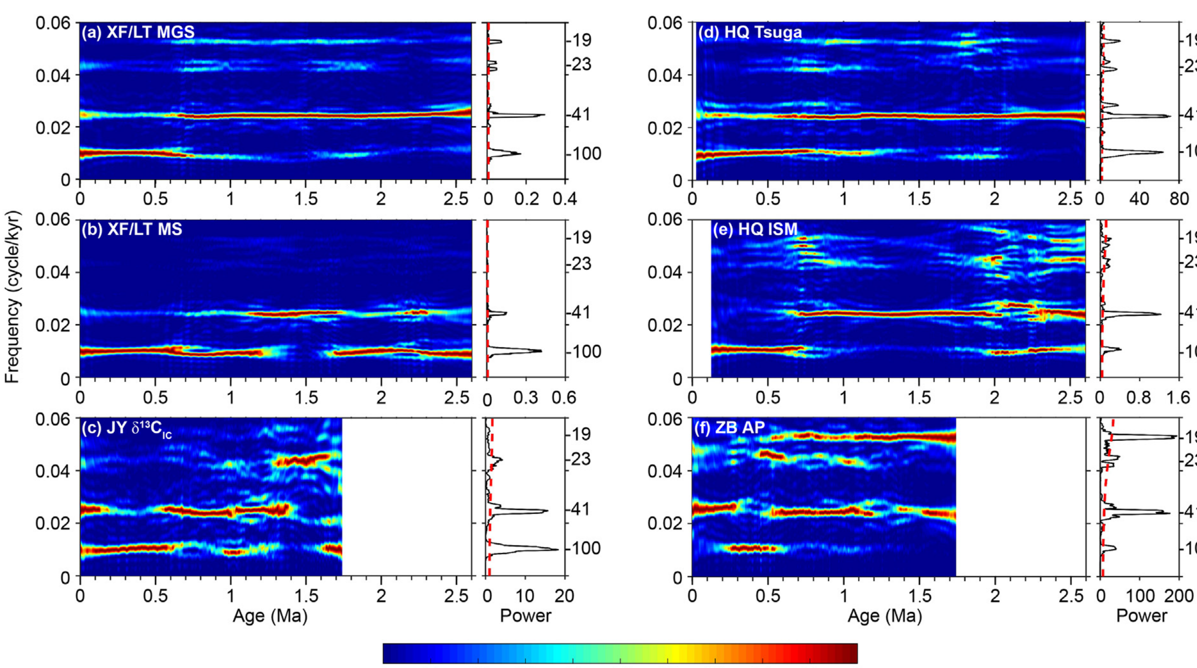

Fig. 5. Evolutionary power spectra of loess and lake proxies. Left panel: (a) MGS and (b) MS of XF/LT (Sun et al., 2006a), (c) JY $\delta^{13}C_{IC}$ (Sun et al., 2019); Right panel: (d) HQ *Tsuga* content and (e) ISM index (An et al., 2011), (f) ZB AP abundance (Zhao et al., 2020). These data sets were preprocessed to isolate the 100-, 41-, and 21-kyr components using band-passing filters with central frequencies of 0.01, 0.025, and 0.05/kyr and bandwidths of 0.002, 0.005, and 0.01/kyr before performing the spectral analyses. Red dashed lines in the power spectra indicate 95% confidence level. (For interpretation of the references to colour in this figure legend, the reader is referred to the Web version of this article.)

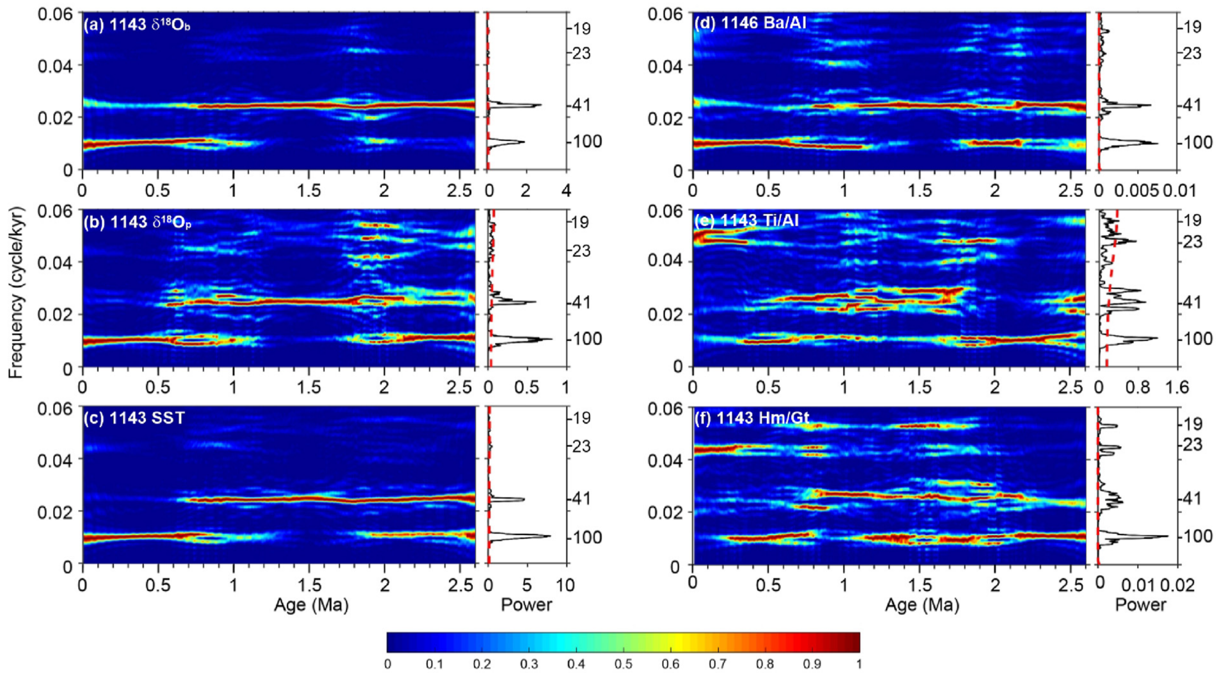

Fig. 6. Evolutionary power spectra of six proxies from two marine cores. Left panel: (a) $\delta^{18}O_b$, (b) $\delta^{18}O_p$, and (c) SST of ODP site 1143 (Tian et al., 2002; Li et al., 2011); Right panel: (d) Ba/Al ratio of ODP site 1146 (Clemens et al., 2008), (e) Ti/Al and (f) Hm/Gt ratios of ODP site 1143 (Zhang et al., 2009; Tian et al., 2011). Data sets were preprocessed to isolate the 100-, 41-, and 21-kyr components before performing the spectral analyses. Red dashed lines in the power spectra indicate 95% confidence level. (For interpretation of the references to colour in this figure legend, the reader is referred to the Web version of this article.)

and ice/CO_2 forcing were persistent during the Quaternary. Type 3 (JY $\delta^{13}C_{IC}$) exhibits a shift from 23-kyr to mixed 100-, 41- and 23-kyr cycles, indicating a shift from the dominant insolation forcing to combined insolation and ice/CO_2 forcing across the MPT. Type 4 (Ti/Al and Hm/Gt ratios of ODP1143 sediments) exhibits persistent 100-, 41-, and 23-kyr cycles without significant periodicity shift through the Quaternary implying complicated roles of glacial and/or eccentricity forcing in driving Quaternary climate change.

We found that proxy records (Type 1) associated with changes in annual temperature and winter wind usually display a traditional MPT from 41-kyr to 100-kyr cycles during 1.2–0.7 Ma. However, proxy records related to monsoon-induced precipitation and weathering processes (Types 2–4) exhibit a diverse manifestation of the MPT from mid-latitude lake and loess sediments to low-latitude marine and terrestrial sediments. For example, the JY $\delta^{13}C_{IC}$ and ZB AP% are highly sensitive to vegetation changes in the monsoon-affected region (Sun et al., 2019; Zhao et al., 2020), displaying strong precession cycles during the early Pleistocene. In the low-latitudes, chemical weathering indicators from terrestrial sediments (e.g. Hm/Gt and Ti/Al ratios) are sensitive to monsoon-induced weathering intensity over the southern Asia (Zhang et al., 2007; Ao et al., 2011; Tian et al., 2011), demonstrating a persistent 100-kyr periodicity during the Quaternary. In addition, persistent 400-ka cyclicity has been inferred from stable carbon isotopes of the South China Sea sediments (Wang et al., 2003) and magnetic parameter of the Tengger Desert sediments (Liu et al., 2021). Continued obliquity pacing was identified in the Sr/Ca ratio of microcodium in loess deposit (Li et al., 2016), whilst dominant precession cycles were identified in the Chinese speleothem $\delta^{18}O$ records (Wang et al., 2008; Cheng et al., 2016). We group these three proxy records as a unique type (Type 5), as only one periodicity persistently dominated through the Quaternary. Regardless of the type, mechanisms underlying these diverse manifestations still need further assessments by direct proxy-model comparison.

4. Sensitivity experiments and seasonal-latitudinal climate characteristics in East Asia

4.1. Sensitivity experiments

The relative sensitivity of the ISM and EAM to changes in orbital parameters, ice volume, and CO_2 have been addressed quantitatively using an emulator approach based on 61 sensitivity experiments performed by the HadCM3 model (Araya–Melo et al., 2015; Sun et al., 2019; Lyu et al., 2021). The same experiments and emulator approach are used here to quantitatively address different sensitivities of temperature, precipitation, southerly wind (V-wind) changes to orbital parameters, CO_2, and ice volume. HadCM3 is an atmosphere-ocean fully coupled general circulation model (Gordon et al., 2000). The assessment of multi-model simulation on East Asian climate shows that HadCM3 can well simulate the annual and seasonal surface air temperature and precipitation climatology in East Asia (Jiang et al., 2005). The HadCM3 model has also been shown to capture reasonably well the monsoon–ENSO interaction and natural variability of the summer rainfall over China (Li et al., 2007; Lei et al., 2014).

The 61 sensitivity experiments on which the emulator is built are designed to sample efficiently changes in three astronomical parameters, CO_2 concentrations, and Northern Hemisphere glaciations experienced during the Quaternary (for a detail experiment design, see Table 1 in Araya–Melo et al., 2015). In order to generate a forcing-response scenario spanning the Quaternary, three astronomical parameters (eccentricity, obliquity, and precession) are used (Berger and Loutre, 1991), and the benthic $\delta^{18}O$ stack (Lisiecki and Raymo, 2005) is scaled as ice level 1–12 to represent different glacial height and volume (Singarayer and Valdes, 2010). The CO_2 concentration over the past 0.8 Ma is obtained from Antarctic records (Lüthi et al., 2008), and before 0.8 Ma it is calculated by following a linear relationship between the benthic $\delta^{18}O$ stack and

CO_2 concentration over the past 0.8 Ma.

The simulated changes in summer (June-July-August) temperature (T-Summer, air temperature at 1.5 m), summer precipitation (P-summer), near-surface (10 m above the ground) summer southerly wind (V-summer), annual temperature (T-annual), and annual precipitation (P-annual) are the estimated equilibrium responses of the HadCM3 for forcing conditions spanning the Quaternary by steps of 1 kyr. Since precipitation pattern is spatially different between southern and northern China in both modern observation and paleoclimate modeling data (e.g. Ding et al., 2008; Lyu et al., 2021), the simulated results were averaged over six latitudinal zones (i.e. 0-10°N, 10-20°N, 20-30°N, 30-40°N, 40-50°N, and 50-60°N, see dashed rectangles in Fig. 7c and d) between 100 and 120°E to address their sensitivities to astronomical, ice volume and CO_2 forcing. Spatial patterns of surface temperature, precipitation, and 850 hPa wind during the boreal summer season in the HadCM3 Pre-industrial simulation are similar to those from the Twentieth Century Reanalysis (20CR) Data during 1836–1865 (Compo et al., 2011; Slivinski et al., 2019), suggesting that the HadCM3 can well simulate the climate change in East Asia (Fig. 7).

4.2. Pre-industrial seasonal changes of temperature, precipitation and southerly wind

Model results reveal that seasonal changes in precipitation, temperature and southerly wind are spatially different over the six latitudinal zones under the pre-industrial condition (Fig. 8). Precipitation changes in five zones all show distinct seasonal cycles with high in summer and low in winter, except for the low-latitude ocean (0-10°N). From south to north, seasonal contrasts of precipitation at 10-30°N are significantly greater than those at 30-60°N. The rainy season is relatively long lasting from April to

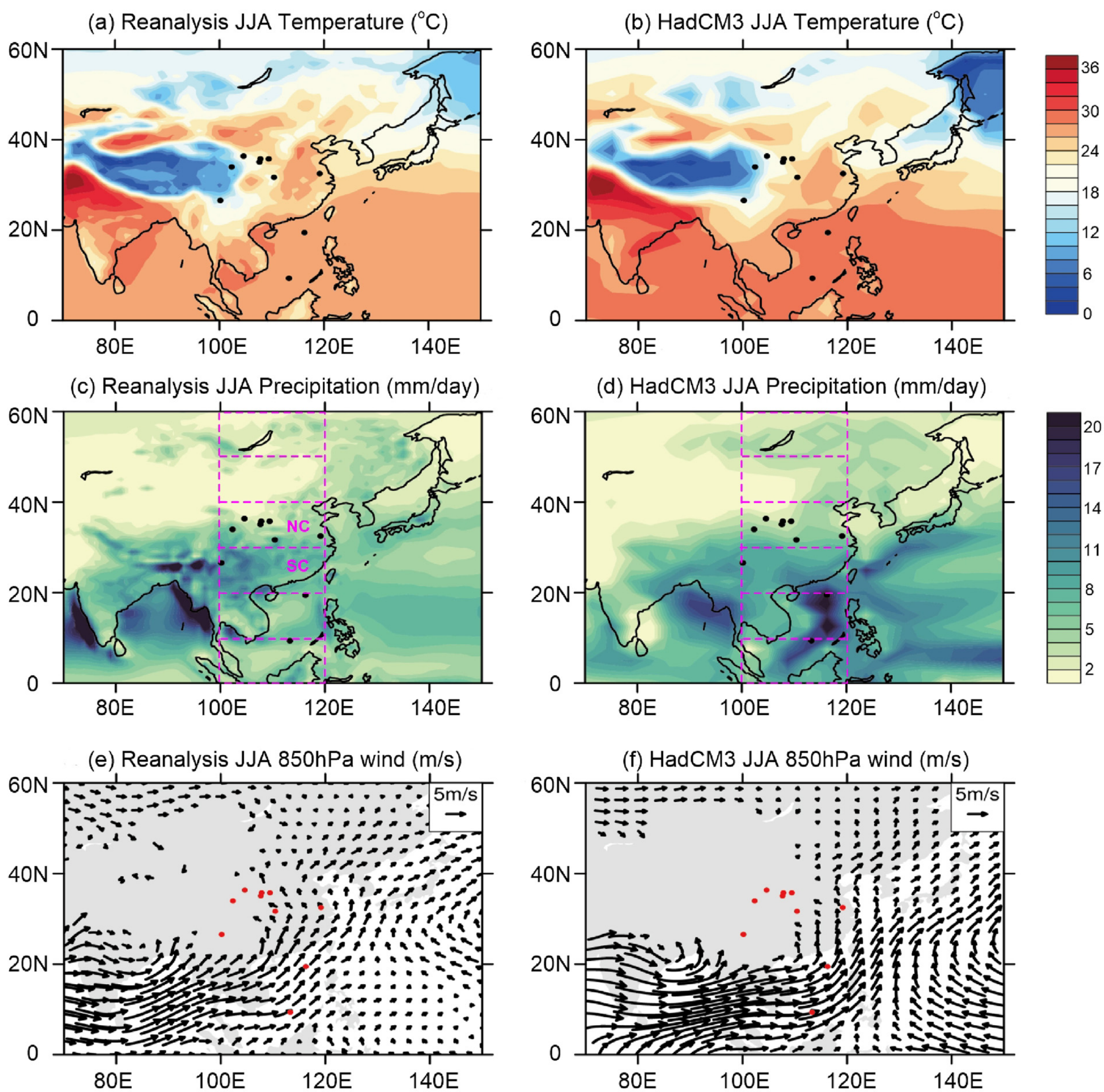

Fig. 7. Comparison between surface temperature (a, b), precipitation (c, d), and 850 hPa wind (e, f) during the boreal summer (JJA, June-July-August) from reanalysis data during 1836–1865 (left panel, *Compo* et al., *2011*; *Slivinski* et al., *2019*) and from the HadCM3 Pre-Industrial simulation (*Araya–Melo* et al., *2015*). Also shown are the six zonal boxes and the location of ten representative proxy records (dots). NC and SC denote the North (30-40°N, 100-120°E) and South (20-30°N, 100-120°E) China, respectively.

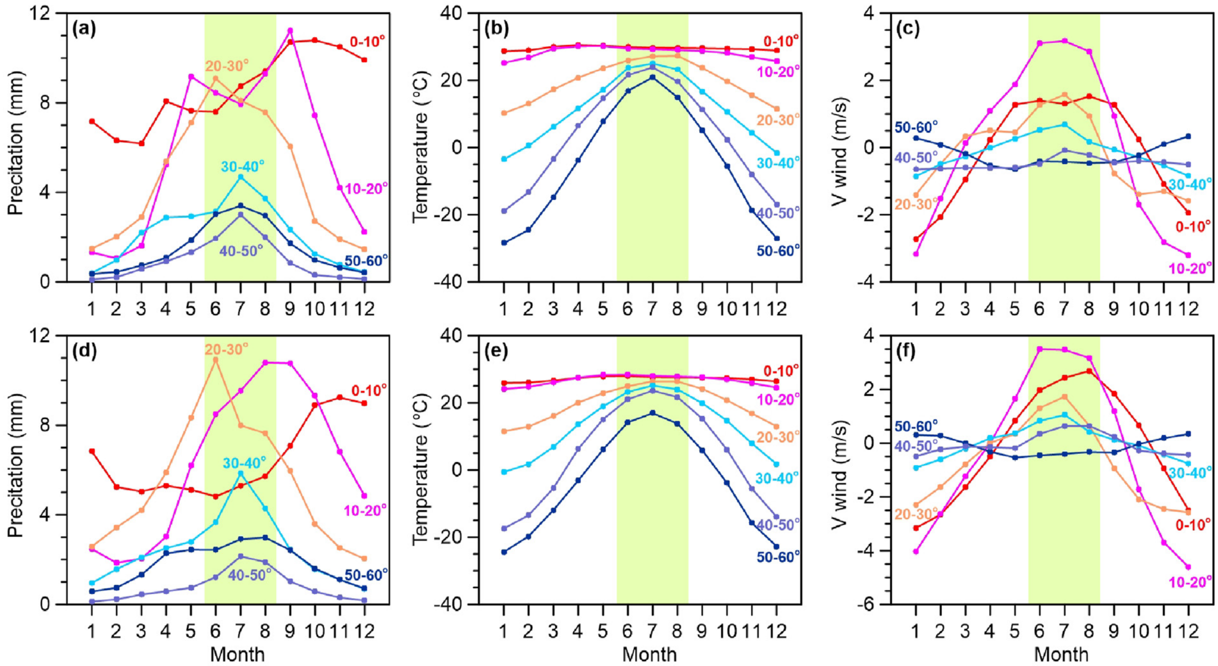

Fig. 8. Seasonal cycles of precipitation, temperature, and southerly wind (V-wind) over six latitudinal zones (0-60°N, 105-120°E) in the East Asian monsoon domain. (a–c) Model data from the HadCM3 Pre-industrial simulation, (d–f) Reanalysis data from the NOAA-CIRES-DOE Twentieth Century during 1836–1865 (Compo et al., 2011; Slivinski et al., 2019).

September at 10-30°N, compared to those concentrated in June to August at 30-60°N. The seasonal characteristic of temperature variation is opposite to that of precipitation change, displaying gradually increasing amplitudes from low latitudes to high latitudes. In the two low-latitude zones of 0-20°N, the seasonal contrast of temperature is less than 5 °C. From 20°N north, the seasonal variation of temperature gradually increases from 15 to 50 °C. Such a spatial pattern in seasonal temperature changes is mainly related to winter temperature difference, because the difference in summer temperature is less than 10 °C over the six latitudinal zones (Fig. 8b).

The southerly wind intensity in summer season can be regarded as a direct indicator of the summer monsoon strength (Liu et al., 2014). Seasonal variations of southerly wind intensity over six latitudinal zones suggest that the summer monsoon influence is more significant at 0-40°N than at 40-60°N (Fig. 8c), consistent with the northern limit of summer monsoon front around 40-45°N (Ding and Chan, 2005). Seasonal variations of southerly wind intensity in low-latitude region (0-10°N) are significantly higher than that in mid-latitude regions (30-40°N). In the area north of 40°N, seasonal variation of southerly wind is not obvious, while the easterly wind shows obvious seasonal reversal. Seasonal changes in precipitation and southerly winds intensity are coupled in the low-latitude (10-20°N) ocean and mid-latitude (20-40°N) land, implying that middle-to-low latitudes of East Asia (10-40°N) are sensitive to changes in both monsoonal wind and precipitation.

To further evaluate the model performance in East Asia, seasonal changes in precipitation, temperature, and southerly wind from the 20CR data during 1836–1865 (Compo et al., 2011; Slivinski et al., 2019) is compared with those from the HadCM3 Pre-industrial simulation (Fig. 8d–f). In general, HadCM3 reproduces well the seasonal and latitudinal changes in precipitation, temperature, and southerly wind in East Asia. The amplitude difference between the model outputs and reanalysis data is only evident for the summer precipitation in 0–10°N, since this domain includes a large fraction of ocean. Unlike the summer season in East Asia is dominated by summer monsoon, the winter season is jointly affected by the winter monsoon and westerly circulation, and characterized by less precipitation and lower temperature. In order to focus more on the debatable dynamics of the Asian summer monsoon, the characteristics of climatic elements during the winter season will not be detailed in the following section.

5. Dynamics of orbital-scale monsoon change in East Asia

5.1. *Outstanding issues of orbital-scale monsoon dynamics*

Orbital-scale monsoon changes are primarily driven by changes in insolation, ice volume, atmospheric concentrations of greenhouse gases, interhemispheric thermal and pressure gradients induced by Earth's orbital parameters (e.g. An et al., 1991a, 2011, 2015; Ding et al., 1995; Wang et al., 2017; Cheng et al., 2021; Clemens et al., 2021). The periodic variations of three astronomical parameters lead to seasonal changes in incoming solar radiation received at Earth's surface (Berger, 1978), producing disparate land-sea thermal and pressure contrasts that drive the monsoon variability (Kutzbach and Guetter, 1986; Prell and Kutzbach, 1987). Meanwhile, the NHIS modulates the strength of monsoon circulations through meridional temperature gradient between high- and mid-latitude regions (An et al., 2001; Wen et al., 2016; Shi et al., 2021b), as well as atmospheric teleconnection induced by ice sheet topography (Yin et al., 2008, 2009). Concentrations of greenhouse gases (particularly CO_2) also influence monsoon variability by affecting temperature gradient between high- and low-latitude regions and migration of the intertropical convergence zone (ITCZ) (Felzer et al., 1998; Lu et al., 2013; Geen et al., 2020). Impacts of these forcing factors on monsoon variability have been individually evaluated by proxy records (e.g. Guo et al., 2012; Sun et al., 2015) and modeling results (Yin et al., 2008, 2009; Wen et al., 2016).

Quantitative reconstructions in paleo-precipitation and temperature changes have provided in-depth understanding of orbital-scale monsoon dynamics (Peterse et al., 2014; Thomas et al., 2016; Beck et al., 2018; Gebregiorgis et al., 2018; Lu et al., 2019; Clemens et al., 2018, 2021). Meanwhile, model simulations can assess the responses of monsoon intensity to the individual and combined effects of astronomical, ice, and CO_2 forcing (Yin et al., 2009; Lu et al., 2013; Liu et al., 2014; Wen et al., 2016; Lyu et al., 2021). Direct comparisons of proxy records with model results (e.g. TRACE21, HadCM3) have also provided further assessments of orbital-scale monsoon dynamics (e.g., Liu et al., 2014; Sun et al., 2019; Cheng et al., 2021). However, deciphering orbital-scale monsoon dynamics still faces three complex problems: (1) Which indicators can truly represent the monsoon intensity; (2) Which region is most sensitive to monsoon changes? (3) How to quantify the responses of monsoon-related climate elements to insolation, ice volume, and CO_2 forcing? To further disentangle these complexities, we extend direct comparison of proxy variability with model results back to the entire Quaternary to facilitate the dynamical understanding of orbital-scale monsoon variability.

5.2. Impacts of different forcing on temperature, precipitation and southerly wind changes

The remarkable feature of the monsoon climate in East Asia is the strong coupling between heavy rainfall and high temperature in the summer season. However, it is often difficult to distinguish the effects of summer or annual temperature and precipitation on these proxy indicators. Therefore, five climate variables (i.e. T-summer, P-summer, V-summer, T-annual, and P-annual) are analyzed to quantify different effects of astronomical parameters, CO_2 and ice volume. The response sensitivities of these five variables were calculated over six latitudinal zones at two intervals of 2−1.2 Ma and 0.8−0 Ma. The major differences of these forcing factors across the MPT are the ice extent and CO_2 concentration during glacial periods (Lisiecki and Raymo, 2005; Hönisch et al., 2009; Araya−Melo et al., 2015). Thus sensitivity analyses were based on full glacial-interglacial ranges of the ice levels (1−12) and CO_2 concentrations (180−280 ppmv) after the MPT and half ranges of the ice levels (1−6) and CO_2 concentrations (220−280 ppmv) before the MPT. The sensitivity index of one forcing parameter is calculated in the following steps. First, we fixed it at its actual value and computed the precipitation variance obtained by varying the other parameters before and after the MPT. Second, this variance over the different values of the aimed parameter was averaged to obtain a mean variance. Third, the sensitivity magnitude was defined as the mean variance divided by the full variance. The rationale, computational methods, and effective applications of sensitivity analysis have been detailed in Oakley and O'Hagan (2004) and Araya−Melo et al. (2015).

The relative impacts of different factors can be assessed by the magnitude of sensitivity. The sensitivity results show that the precession, obliquity, CO_2, and ice play different roles in affecting these climate variables. After the MPT (Post-MPT)**,** precession is the dominant factor affecting three summer climate variables, while obliquity only plays limited influence on T-summer and P-summer at 30-60°N (Fig. 9a-c). Compared to two astronomical parameters, CO_2 has a weak effect on T-summer, but hardly affects P-summer and V-summer changes. Ice volume has a relatively small effect on T-summer, and its impact on V-summer wind is mainly manifested at 0-10°N and 40-60°N. Moreover, ice volume significantly affects the P-summer change at 0-30°N. Before the MPT (Pre-MPT), precession played a more dominant role in affecting the summer climate variables than the other three forcing factors (Fig. 9f-h). The relative effects of both CO_2 and ice sheets were strongly weakened, due to increased CO_2 concentration and decreased ice extent during the moderate glaciations before the MPT.

For the T-annual and P-annual changes, relative roles of these four forcing are quite different from those for the summer variables. After the MPT, the T-annual change is mainly affected by CO_2 and precession, and the impact of CO_2 is greater than precession (Fig. 9d). Ice volume only affects the T-annual over northern regions (30-60°N). The P-annual change (Fig. 9e), however, is mainly affected by precession and ice volume, and less influenced by obliquity and CO_2. In the southern region (0-30°N), the P-annual is mainly affected by ice volume change, whereas in the northern region (30-60°N), the P-annual is jointly affected by precession, obliquity, CO_2, and ice forcing, with precession being the dominant driving factor. Before the MPT, the impact of precession on T-annual is greater than those of CO_2 and ice volume (Fig. 9i). The precession's effect on P-annual is more evident than the ice volume in the northern region (30−60°N), but its influence becomes relative weaker than ice volume in the southern region (0-30°N) (Fig. 9j). In summary, precession plays a dominant role in affecting summer climate variables, whereas ice volume and CO_2 play separately roles in affecting the P-annual and T-annual changes.

The mechanisms that drive the East Asian summer monsoon include both insolation-, ice volume-, and CO_2-induced changes in both atmospheric circulations and oceanic processes (e.g. Lu et al., 2013; Liu et al., 2014; An et al., 2015; Wen et al., 2016), including the land-sea pressure gradient, southerly wind, atmosphere moisture content, and the migration of the ITCZ. Model results from the same HadCM3 sensitivity experiments show that large-scale surface cooling induced by increased ice volume and CO_2 concentrations during post-MPT glaciations can significantly reduce the land-ocean pressure contrast and weaken the summer monsoon circulation and the water vapor flux from the Northwest Pacific (Lyu et al., 2021). Before the MPT, changes in ice sheets and CO_2 can cause similar anomalous patterns in pressure, winds and temperature, but the magnitude of changes is smaller than in extreme glaciations after the MPT. Decreased sensitivity of monsoonal hydroclimate to insolation forcing as the Northern Hemisphere became increasingly glaciated during the Pleistocene can result in the periodicity shift across the MPT (Sun et al., 2019).

6. Regional sensitivity to astronomical, ice volume, and CO_2 forcing

6.1. Spatial differences in response to astronomical, ice volume, and CO_2 forcing

Meteorological observation data reveal that the spatial pattern of the inter-decadal variability of summer precipitation in China is mainly structured with two meridional modes: the dipole (southern vs. northern China) pattern and the sandwich (southern China-Yangtze River valley-northern China) pattern (Ding et al., 2008). Proxy records and model results also reveal similar spatial patterns of precipitation (i.e. Liu et al., 2014; Zhang et al., 2018a). Our modeling results reveal that the impacts of four driving factors on temperature and precipitation changes are spatially different after the MPT. The influences of precession on T-summer are most significant in mid-latitude regions (20-40°N) (Fig. 9a), and its influence on T-annual gradually increases from low-latitude to mid-latitude regions (Fig. 9d). The influence of precession on summer and annual precipitation is significantly stronger in three northern zones (30-60°N) than in the southern zones (0-30°N) (Fig. 9c and e). Obliquity slightly affects T-summer, P-summer, and P-annual in the northern zones. CO_2 has distinct effects on T-summer in the southern zones and P-annual in the northern zones. Ice volume has a greater impact on P-summer and P-annual in the south than in the north, since the ice sheet plays an important role in the ITCZ migration (Lyu et al., 2021). Meanwhile, the impact of ice volume on

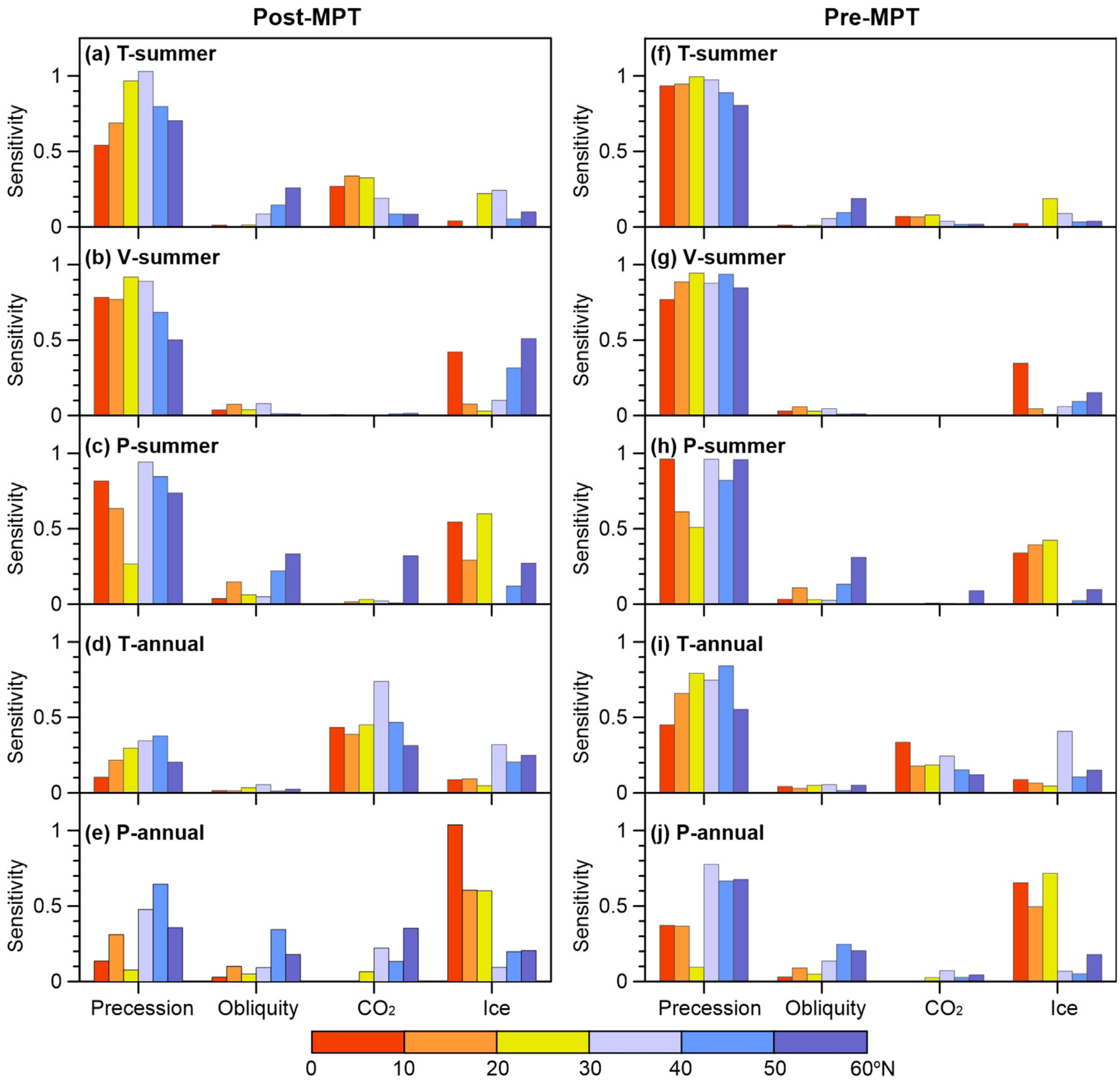

Fig. 9. Sensitivity of five climate variables to precession, obliquity, CO_2, and ice forcing. Left panel (a–e): sensitivities of summer temperature, summer southerly wind, summer precipitation, annual Temperature, and annual precipitation over six latitudinal zones (0-60°N) in East Asia after the MPT (Post-MPT); Right panel (f–j): sensitivities of these variables before the MPT (Pre-MPT).

T-annual is greater in the northern zones than in the southern part.

The spatial differences of the sensitivity results in response to these four forcing factors are slightly different before and after the MPT. Before the MPT, the influence of precession on T-summer is spatially consistent, whereas its influences on summer and annual precipitations are stronger in the northern zones than in the southern regiones. The influence of ice volume on summer and annual precipitation is stronger in three southern zones than in the northern parts. Due to the relatively low ice volume and high CO_2 concentration during glacial times before the MPT, the relative influences of CO_2 on temperature and ice on precipitation are evidently weakened. Clearly, the sensitivities of temperature and precipitation responses to astronomical, ice and CO_2 forcing are spatially different between north and south at 30°N. Such a north-south difference is particularly evident for the precipitation response. Therefore, we will consider the regional response differences to further discuss orbital-scale climate variability and mechanisms in the follow section.

6.2. Comparison between simulated results in north and south China

Simulated changes of five climate variables spanning the last 2.6 Ma are compared between two sensitive regions (South China, 20-30°N; North China, 30-40°N) (Fig. 10). T-summer in South China is generally higher than that in North China, but its varying magnitude is smaller than that in North China. T-summer changes in the two regions are predominantly controlled by the precession-induced summer insolation. The V-summer changes in the two regions are also dominated by precession cycles, while the intensity and variability of V-summer in South China are significantly higher than those in North China. By contrast, the P-summer changes in

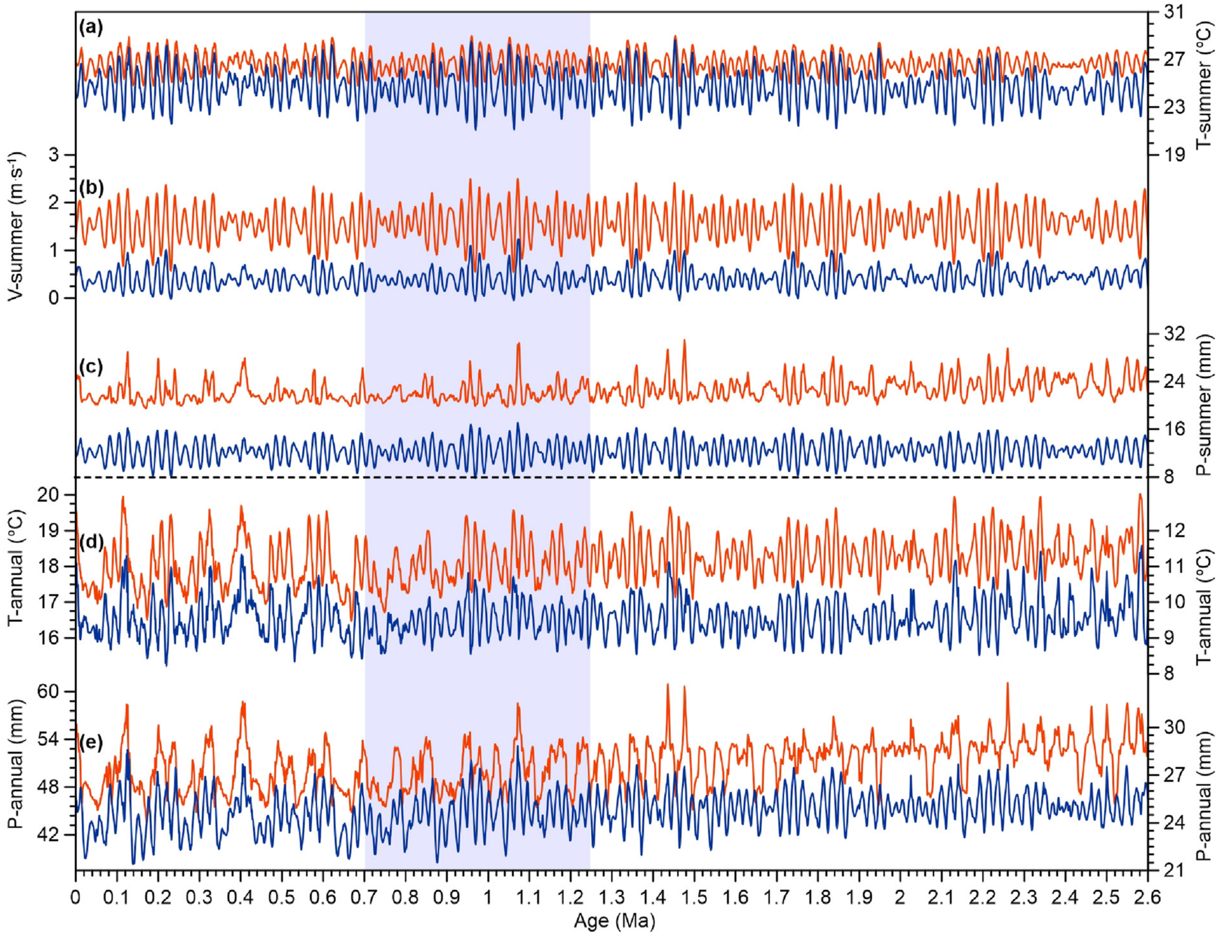

Fig. 10. Simulated summer (a–c) and annual (d, e) changes in temperature, southerly wind and precipitation over north (30-40°N, blue lines) and south China (20-30°N, red lines). (For interpretation of the references to colour in this figure legend, the reader is referred to the Web version of this article.)

the two regions are quite different. The P-summer in South China is relatively high and exhibits significant variability at both glacial-interglacial and precession time scales, whereas the P-summer in North China is less variable but dominated by precession cycles. Changes of P-summer and V-summer in North China are quite highly correlated, whereas variations of these two variables are decoupled in South China. Changes in T-annual and P-annual are generally similar in the two regions. The amplitude and variability of these two variables in South China are larger than those in North China. The T-annual and P-annual vary from 8.5 to 11.5 °C and 21–28 mm in North China to 17-20 °C and 45–60 mm in South China, respectively.

Evolutionary power spectra of these simulated climate variables are presented to further decipher regional differences in the evolving orbital periodicities (Fig. 11). Spectra of the T-summer and V-summer in these two regions are dominated by consistently strong precession cycles. P-summer in North China is also dominated by persistent precession cycles, but exhibits a mixing pattern of 100, 41, 23 and 19-kyr periodicities in South China. The T-annual spectra are similar between these two regions, characterized by strong precession and weak obliquity cycles over the last 2.6 Ma and a significant 100-kyr cycle after 0.7 Ma (Type 2). The P-annual spectra, however, are apparently different between North and South China. The P-annual in North China is dominated by persistent precession cycles over the last 2.6 Ma and a strong 100-kyr cycle since 0.7 Ma (Type 3), implying a strong influence of ice volume after the MPT. In South China, P-annual spectrum shows a strong 41-kyr cycle between 2.6 and 0.7 Ma and a dominant 100-kyr period after 0.7 Ma, implying that the ice volume played a significant impact on the annual precipitation.

The simulation results show that different climate variables can indeed exhibit diverse manifestations of orbital-scale changes through the Quaternary. Similar to the five types of orbital-scale variability inferred from proxy records, the simulated climate variables over two regions can be grouped into four types. P-annual in South China share similar evolving spectrum as the Type 1 (Fig. 11j). Evolutionary power spectra of P- summer and T-annual in South China are identical to that of Type 2, characterized by a shift from 41/23-kyr to 100/41/23-kyr cycles (Fig. 11h and i). P-annual in North China displays a period shift from persistent 23-kyr through the Quaternary to 100/23-kyr cycles after 0.7 Ma (Type 3, Fig. 11e). The other five variables (T-summer and V-summer in both regions, and P-summer in North China) corresponding to Type 5 dominated by persistent precession cycles. It's noteworthy that model results don't exhibit persistent 400-, or 100-kyr cycles throughout the Quaternary. 41-kyr cycles are more evident in the P-summer, T-annual, and P-annual over south China than north China, but very weak in T-summer and V-summer over both north and south China.

6.3. Implications of proxy-model comparison

To assess the sensitivity of different proxies to climate variables, proxy indicators from lake, loess and stalagmite records are directly compared with simulated temperature and precipitation changes.

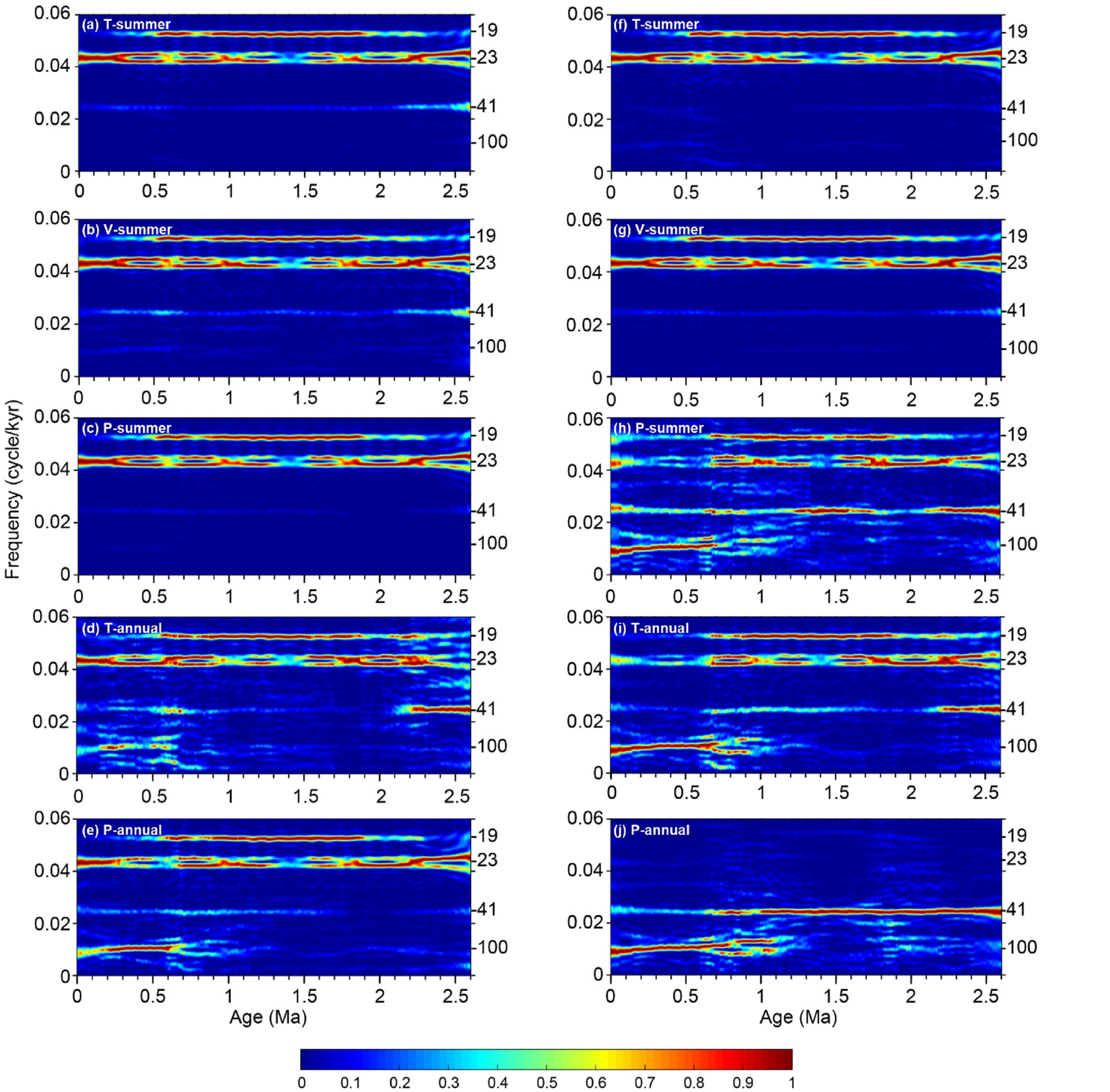

Fig. 11. Evolutionary power spectra of six simulated climate variables over north (30-40°N, left panel) and south (20-30°N, right panel) China. From top to bottom: (a, f) summer temperature, (b, g) summer southerly wind, (c, h) summer precipitation, (d, i) annual temperature, and (e, j) annual precipitation.

Comparison of three proxies from HQ paleolake with the simulation results at 20-30°N suggested that *Tsuga* content, TOC content, and ISM index likely respond well to changes in annual temperature, summer precipitation, and annual precipitation, respectively (Fig. 12a–c). The *Tsuga* content mainly reflects the annual temperature range, which is strongly associated with the winter temperature change (An et al., 2011). Therefore, the *Tsuga* content exhibits similar variability to the simulated T-annual change, in terms of both amplitude and rhythms. The TOC content in the Heqing paleolake is sensitive to monsoon-induced biomass change in the lake catchment particularly during the interglacial periods, and thus matches well with the simulated P-summer change. By contrast, ISM index can capture both glacial weakening and interglacial strengthening of the monsoon intensity, and thus corresponds well to the P-annual change. Wavelet coherence spectra suggest that these three proxy records are strongly coupled with changes in T-annual, P-summer and P-annual, respectively (Fig. 12d–f). Strong coherency at 100-kyr period after the MPT confirms the significant ice effects on the P-summer and P-annual, and ice/CO_2 effects on T-annual in South China. The coherency at precession band is evident in the *Tsuga*/T-annual and TOC/P-summer spectra, but unclear in the ISM/P-annual spectrum, implying different impacts of insolation on temperature and precipitation changes in the same region.

Since the age models for loess, lake, and stalagmite records are established by different approaches, the chronological uncertainties make it difficult to perform a cycle-by-cycle correlation between the proxies and model results. Nevertheless, good match

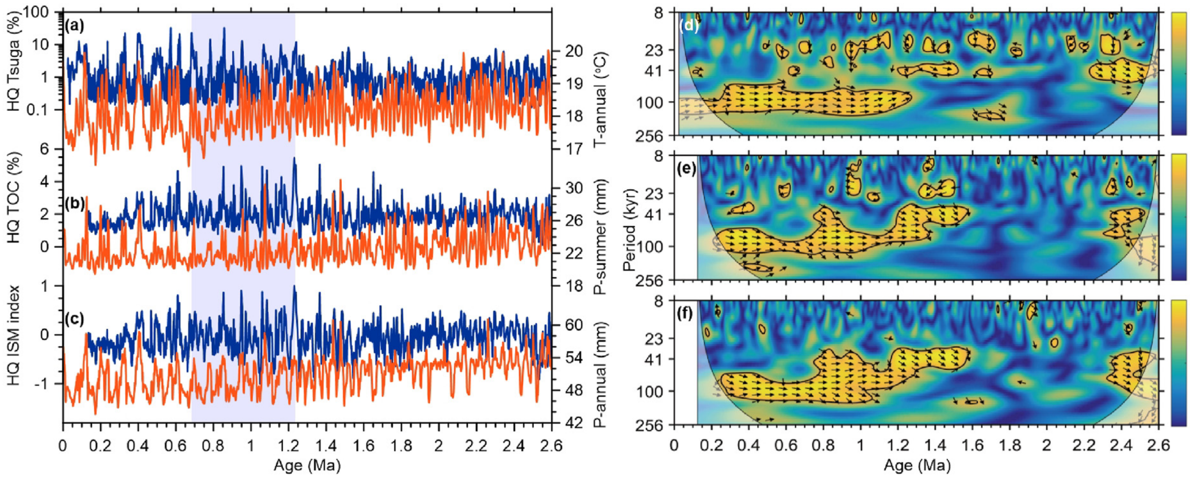

Fig. 12. Comparison of simulated temperature and precipitation changes (red lines) at 20-30°N with three proxy records (blue lines) from HQ Paleolake (An et al., 2011) and their corresponding wavelet coherence spectra. (a, d) annual temperature vs. *Tsuga* content, (b, e) summer precipitation vs. TOC content, and (c, f) annual precipitation vs. ISM index. (For interpretation of the references to colour in this figure legend, the reader is referred to the Web version of this article.)

between these proxy records with the simulation results at 30-40°N suggests that ZB AP concentration, cave $\delta^{18}O$ and loess $\delta^{13}C_{IC}$ are sensitive to changes in T-annual, P-summer, and P-annual, respectively (Fig. 13a–c). The AP content in the ZB sediments shows significant glacial-interglacial variability after 0.6 Ma, consistent with the simulated T-annual change. However, marked decrease in the AP content after 0.6 Ma than before, especially during the glacial times, is not evident in the simulated T-annual change. Variation of the composite $\delta^{18}O$ records from Hulu/Sanbao caves is quite similar to the simulated P-summer change, characterized by dominant precession cycles, but lags to the P-summer by 90°, indicating other forcing factors are also involved. The loess $\delta^{13}C_{IC}$ variability is very similar to the simulated P-annual change, showing distinctive shifts from dominant precession cycles to combined glacial-interglacial and precessional fluctuations across the MPT. Coherency spectra between these three proxies and simulated results reveal that precession and ice/CO_2 forcing jointly affect orbital-scale changes in annual temperature and precipitation changes in North China, whereas summer precipitation is predominantly driven by precession-induced insolation change (Fig. 13d–f).

The diverse nature of proxy fluctuations and model results during the Quaternary can be attributed to two major reasons: (1) different sensitivities of proxy indicators to precipitation and temperature changes, and (2) different responses of temperature and precipitation changes to external (insolation) and internal (ice volume) forcing. Formation of Chinese loess-paleosol sequences is not only related to ice volume-induced changes in source aridity and winter monsoon intensity (An et al., 1991a; Ding et al., 1995), but also influenced by precipitation-induced changes in pedogenesis and chemical weathering (An et al., 1991b; An, 2000). Therefore, Chinese loess can simultaneously document both 100-kyr cycles of the source aridity and winter monsoon intensity coupled with the NHIS change and 21-kyr signal of hydroclimate change associated with insolation-driven changes in land-ocean thermal and pressure gradients. Stalagmites, however, are greatly influenced by the hydroclimate change, thus its $\delta^{18}O$ values likely reflect combined changes in precipitation, large-scale changes in monsoon

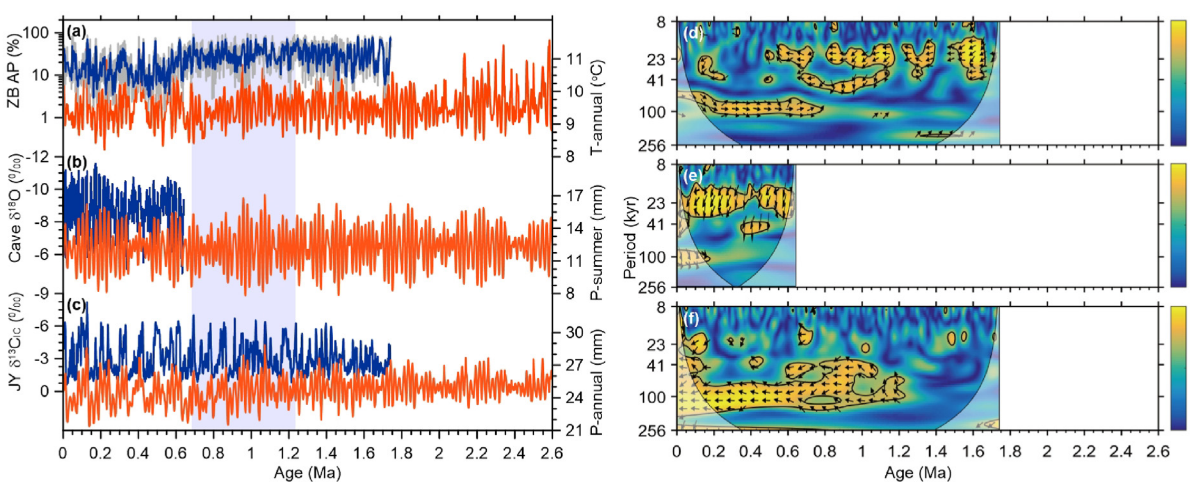

Fig. 13. Comparison of simulated temperature and precipitation changes (red lines) with lake-, loess- and spaleothem-based proxies (blue lines) from 30 to 40°N and their corresponding wavelet coherence spectra. (a, d) annual temperature vs. AP% (11-points smoothing) from the Zoige basin (Zhao et al., 2020), (b, e) summer precipitation vs. $\delta^{18}O$ from the Hulu/Sanbao caves (Wang et al., 2008; Cheng et al., 2016), and (c, f) annual precipitation vs. $\delta^{13}C_{IC}$ from the JY loess (Sun et al., 2019). (For interpretation of the references to colour in this figure legend, the reader is referred to the Web version of this article.)

circulation and moisture sources (Wang et al., 2001, 2008; Clemens et al., 2010, 2018; Cai et al., 2015; Cheng et al., 2016, 2021). In north China, simulated changes in summer precipitation and southerly wind are strongly coupled. Therefore, different cyclicities between JY $\delta^{13}C_{IC}$ and speleothem $\delta^{18}O$ is related to the intrinsic characteristics of the two proxy records (i.e. summer vs. annual precipitation), rather than controversial orbital-scale monsoon dynamics.

7. Conclusions and prospects

Representative proxy records from loess, stalagmite, lake, and marine sediments have been synthesized to address the spatio-temporal patterns of Quaternary climate change in East Asia. Changes in loess grain size, sea surface temperature, benthic and planktonic oxygen isotopes in the South China Sea sediments show strong 100-kyr cycles after the MPT, since they are sensitive to ice volume and/or CO_2 forcing. In contrast, several hydroclimatic and terrestrial weathering proxies (e.g. loess $\delta^{13}C_{IC}$, lake proxies, and mineral/chemical compositions of South China Sea sediments) are characterized by strong 23-kyr cycles or mixed 41-kyr and 23-kyr cycles, together with distinct 100-kyr cycles after the MPT. The coexistence of 100-, 41-, and 23-kyr cycles illustrates the combined effects of astronomical, ice volume, and CO_2 forcing on Quaternary monsoon change in East Asia. Modeling results suggest that responses of temperature and precipitation to insolation, ice, and CO_2 forcing are spatially different. In North China (30-40°N), insolation plays a predominant role in driving temperature and precipitation changes during the summer season, while ice and CO_2 play more dominant roles in affecting the annual precipitation and temperature changes, respectively. In South China (20-30°N), responses of different climate variables to four forcing factors are also divergent.

Our proxy-model comparison suggests that insolation, ice, and CO_2 changes jointly affect the Quaternary climate changes in East Asia, but their effects on each climate element are quite different on both seasonal and regional scales. Insolation plays a leading role in affecting changes in temperature, precipitation, and southerly wind during the summer season. In addition to the influence of solar insolation, changes in annual mean temperature and precipitation are also affected to varying degrees by CO_2 and ice volume. Our synthesis suggests that diverse expressions of evolving periodicities in the proxies are attributable to their different responses to precipitation and temperature changes. Meanwhile, different sensitivities of temperature and precipitation to external and internal forcing should be involved when addressing the dynamics of orbital-scale climate change inferred from different proxies from various archives.

To better decipher orbital-scale monsoon changes and dynamics, future work could focus on three aspects. Firstly, high-resolution and quantitative reconstructions of paleotemperature and paleoprecipitation changes (e.g. Beck et al., 2018; Lu et al., 2019) are crucial for differentiating their impacts on proxy indicators. The potential effect of provenance shifts on mineral and geochemical proxies should also be considered when addressing Quaternary climate change using physiochemical indicators. Secondly, transient simulations that incorporate both external forcing and internal feedbacks using high-resolution regional Earth climate system models should be performed to generate more reliable climate variables that capture key features of monsoon climate including the seasonal cycles, interannual variability, and regional diversity (Zheng et al., 2004; Liang et al., 2019). Moreover, multi-scale interactions, e.g. the cumulative effect of the North Atlantic abrupt events and the modulation effect of asynchronous development of bi-polar ice-sheets on orbital-scale climate changes, should be assessed using more sensitivity experiments. Lastly, direct comparisons of quantitatively reconstructed temperature and/or precipitation data with climate variables from Earth climate system models have greatly advanced our understanding of multiscale monsoon dynamics (e.g. Liu et al., 2014; Shi et al., 2021a; Zhang et al., 2022), which should be conducted actively for future assessments of orbital-scale climate change and dynamics in a global context.

Authors' contributions

Youbin Sun, Steven Clemens, and Zhisheng An initiated this work. Ting Wang, Yanjun Cai, and Li Ai collected the proxy records. Qiuzhen Yin, Anqi Lyu, and Michel Crucifix analyzed the modeling results. All authors contributed to data interpretation and preparation of manuscript.

Declaration of competing interest

The authors declare that they have no known competing financial interests or personal relationships that could have appeared to influence the work reported in this paper.

Acknowledgements

We are grateful to two anonymous reviewers, Zhengguo Shi, and Xiaolin Ma for their valuable suggestions. This work was supported by grant from the Chinese Academy of Sciences (No. XDB40000000). A. Lyu is supported by the grants from the UCLouvain and China Scholarship Council (CSC) Grant (#201706190226). Computational resources have been provided by the supercomputing facilities of the Université catholique de Louvain (CISM/UCL) and the Consortium des Équipements de Calcul Intensif en Fédération Wallonie Bruxelles (CÉCI) funded by the Fond de la Recherche Scientifique de Belgique (F.R.S.-FNRS) under convention 2.5020.11.

References

An, Z., 2000. The history and variability of the East Asian paleomonsoon climate. Quat. Sci. Rev. 19, 171–187.
An, Z., Clemens, S.C., Shen, J., Qiang, X., Jin, Z., Sun, Y., Prell, W.L., Luo, J., Wang, S., Xu, H., Cai, Y., Zhou, W., Liu, X., Liu, W., Shi, Z., Yan, L., Xiao, X., Chang, H., Wu, F., Ai, L., Lu, F., 2011. Glacial–interglacial Indian summer monsoon dynamics. Science 333, 719–723.
An, Z.S., Colman, S.M., Zhou, W.J., Li, X.Q., Brown, E.T., Jull, A.J.T., Cai, Y.J., Huang, Y.S., Lu, X.F., Chang, H., Song, Y.G., Sun, Y.B., Xu, H., Liu, W.G., Jin, Z.D., Liu, X.D., Cheng, P., Liu, Y., Ai, L., Li, X.Z., Liu, X.J., Yan, L.B., Shi, Z.G., Wang, X.L., Wu, F., Qiang, X.K., Dong, J.B., Lu, F.Y., Xu, X.W., 2012. Interplay between the westerlies and asian monsoon recorded in lake Qinghai sediments since 32 ka. Sci. Rep. 2, 619.
An, Z., Kukla, G.J., Porter, S.C., Xiao, J., 1991a. Late quaternary dust flow on the Chinese Loess Plateau. Catena 18, 125–132.
An, Z., Kukla, G.J., Porter, S.C., Xiao, J., 1991b. Magnetic susceptibility evidence of monsoon variation on the Loess Plateau of central China during the last 130,000 years. Quat. Res. 36, 29–36.
An, Z., Kutzbach, J.E., Prell, W.L., Porter, S.C., 2001. Evolution of Asian monsoon and phased uplift of the Himalaya-Tibetan plateau since late Miocene times. Nature 411.
An, Z., Liu, T., Lu, Y., Porter, S.C., Kukla, G.J., Wu, X., Hua, Y., 1990. The long–term paleomonsoon variation recorded by the loess–paleosol sequence in central China. Quat. Int. 7/8, 91–95.
An, Z., Wu, G., Li, J., Sun, Y., Liu, Y., Zhou, W., Cai, Y., Duan, A., Li, L., Mao, J., Cheng, H., Shi, Z., Tan, L., Yan, H., Ao, H., Chang, H., Feng, J., 2015. Global monsoon dynamics and climate change. Annu. Rev. Earth Planet Sci. 43, 29–77. https://doi.org/10.1146/annurev-earth-060313-054623.
Ao, H., Dekkers, M.J., Qin, L., Xiao, G., 2011. An updated astronomical timescale for the Plio–Pleistocene deposits from South China Sea and new insights into Asian monsoon evolution. Quat. Sci. Rev. 30, 1560–1575.
Ao, H., Rohlinge, E.J., Stringer, C., Roberts, A.P., Dekkers, M.J., Dupont-Nivet, G., Yu, J., Liu, Q., Zhang, P., Liu, Z., Ma, X., Zhou, W., Jin, Z., Xiao, G., Wang, H., Sun, Q., Yang, P.G., Peng, X., Shi, Z., Qiang, X., An, Z., 2020. Two-stage mid-Brunhes climate transition and mid-Pleistocene human diversification. Earth Sci. Rev. 210, 103354.
Araya–Melo, P.A., Crucifix, M., Bounceur, N., 2015. Global sensitivity analysis of the

Indian monsoon during the Pleistocene. Clim. Past 11, 45–61.
Beck, J.W., Zhou, W., Li, C., Wu, Z.K., White, L., Xian, F., Kong, X.H., An, Z.S., 2018. A 550,000-year record of East Asian monsoon rainfall from ^{10}Be in loess. Science 360, 877–881.
Bemis, B.E., Spero, H.J., Bijma, J., Lea, D.W., 1998. Reevaluation of the oxygen isotopic composition of planktonic foraminifera, Experimental results and revised paleotemperature equations. Paleoceanography 13, 150–160.
Berger, A., 1978. Long-term variations of daily insolation and Quaternary climatic changes. J. Atmos. Sci. 35, 2362–2367.
Berger, A., Loutre, M.F., 1991. Insolation values for the climate of the last 10 million years. Quat. Sci. Rev. 10, 297–317.
Berger, A., Crucifix, M., Hodell, D.A., Mangili, C., McManus, J.F., Otto-Bliesner, B., Pol, K., Raynaud, D., Skinner, L.C., Tzedakis, P.C., Wolff, E.W., Yin, Q., Abe-Ouchi, A., Barbante, C., Brovkin, V., Cacho, I., Capron, E., Ferretti, P., Ganopolski, A., Grimalt, J.O., Hönisch, B., Kawamura, K., Landais, A., Margari, V., Martrat, B., Masson-Delmotte, V., Mokeddem, Z., Parrenin, F., Prokopenko, A.A., Rashid, H., Schulz, M., Riveiros, N.V., 2016. Interglacials of the last 800,000 years. Rev. Geophys. 54, 162–219. https://doi.org/10.1002/2015RG000482.
Berger, A., Imbrie, J., Hays, J., Kukla, G., Saltzman, B., 1984. Milankovitch and Climate. Springer, Dordrecht. https://doi.org/10.1007/978-94-017-4841-4.
Betzler, C., Eberli, G.P., Lüdmann, T., Reolid, J., Kroon, D., Reijmer, J.J.G., Swart, P.K., Wright, J., Young, J.R., Alvarez-Zarikian, C., Alonso-García, M., Bialik, O.M., Blättler, C.L., Guo, J.A., Haffen, S., Horozal, S., Inoue, M., Jovane, L., Lanci, L., Laya, J.C., Hui Mee, A.L., Nakakuni, M., Nath, B.N., Niino, K., Petruny, L.M., Pratiwi, S.D., Slagle, A.L., Sloss, C.R., Su, X., Yao, Z., 2018. Refinement of Miocene sea level and monsoon events from the sedimentary archive of the Maldives (Indian Ocean). Prog. Earth Planet. Sci. 5 (1), 5. https://doi.org/10.1186/s40645-018-0165-x.
Bloemendal, J., Liu, X., Sun, Y., Li, N., 2018. An assessment of magnetic and geochemical indicators of weathering and pedogenesis at two contrasting sites on the Chinese Loess plateau. Palaeogeogr. Palaeoclimatol. Palaeoecol. 257, 152–168.
Boulay, S., Colin, C., Trentesaux, A., Frank, N., Liu, Z., 2005. Sediment sources and East Asian monsoon intensity over the last 450 ky. mineralogical and geochemical investigations on south China sea sediments. Palaeogeogr. Palaeoclimatol. Palaeoecol. 228 (3–4), 260–277.
Cai, Y., Fung, I.Y., Edwards, R.L., An, Z., Cheng, H., Lee, J.-E., Tan, L., Shen, C., Wang, X., Day, J.A., Zhou, W., Kelly, M.J., Chiang, C.H., 2015. Variability of stalagmite-inferred Indian monsoon precipitation over the past 252,000 y. Proc. Natl. Acad. Sci. U.S.A. 112, 2954–2959. https://doi.org/10.1073/pnas.1424035112.
Caley, T., Malaize, B., Revel, M., Ducassou, E., Wainer, K., Ibrahimd, M., Shoeaibd, D., Migeonc, S., Marieua, V., 2011. Orbital timing of the Indian, East Asian and African boreal monsoons and the concept of a "global monsoon". Quat. Sci. Rev. 30, 3705–3715. https://doi.org/10.1016/j.quascirev.2011.09.015.
Chen, F., Li, J., Zhang, W., 1991. Loess stratigraphy of the Lanzhou profile and its comparison with deep-sea sediment and ice core record. Geojournal 24 (2), 201–209.
Chen, F.H., Chen, J.H., Huang, W., Chen, S.Q., Huang, X.Z., Jin, L.Y., Jia, J., Zhang, X.J., An, C.B., Zhang, J.W., Zhao, Y., Yu, Z.C., Zhang, R.H., Liu, J.B., Zhou, A.F., Feng, S., 2019. Westerlies Asia and monsoonal Asia: spatiotemporal differences in climate change and possible mechanisms on decadal to sub-orbital timescales. Earth Sci. Rev. 192, 337–354.
Chen, J., Farrell, J.W., Murray, D.W., Prell, W.L., 1995. Timescale and paleoceanographic implications of a 3.6 My oxygen isotope record from the northeast Indian Ocean (Ocean Drilling Program site 758). Paleoceanography 10, 21–47.
Cheng, H., Edwards, R.L., Broecker, W.S., Denton, G.H., Kong, X., Wang, Y., Zhang, R., Wang, X., 2009. Ice age terminations. Science 326, 248–252.
Cheng, H., Edwards, R.L., Sinha, A., Spötl, C., Yi, L., Chen, S., Kelly, M., Kathayat, G., Wang, X., Li, X., Kong, X., Wang, Y., Ning, Y., Zhang, H., 2016. The Asian monsoon over the past 640,000 years and ice age terminations. Nature 534, 640–646.
Cheng, H., Zhang, H., Cai, Y., Shi, Z., Hao, Q., Peng, Y., Sinha, A., Li, H., Zhao, J., Tian, Y., Baker, J., Perez-Mejías, C., 2021. Orbital-scale Asian summer monsoon variations: paradox and exploration. Sci. China Earth Sci. 64, 529–544. https://doi.org/10.1007/s11430-020-9720-y.
Clark, P.U., Archer, D., Pollard, D., Blum, J.D., Rial, J.A., Brovkin, V., Mix, A.C., Pisias, N.G., Roy, M., 2006. The middle Pleistocene transition, characteristics, mechanisms, and implications for long–term changes in atmospheric pCO_2. Quat. Sci. Rev. 25, 3150–3184. https://doi.org/10.1016/j.quascirev.2006.07.008.
Clemens, S.C., Holbourn, A., Kubota, Y., Lee, K.E., Liu, Z., Chen, G., Nelson, A., Fox-Kemper, B., 2018. Precession-band variance missing from East Asian monsoon runoff. Nat. Commun. 9, 3364. https://doi.org/10.1038/s41467-018-05814-0.
Clemens, S.C., Kuhnt, W., LeVay, L.J., and the Expedition 353 Scientists, 2016. Indian Monsoon Rainfall. Proceedings of the International Ocean Discovery Program, vol. 353. International Ocean Discovery Program, College Station, TX. https://doi.org/10.14379/iodp.proc.353.2016.
Clemens, S.C., Murray, D.W., Prell, W.L., 1996. Nonstationary phase of the plio–pleistocene asian monsoon. Science 274, 943–948.
Clemens, S.C., Prell, W.L., Murray, D., Shimmield, G., Weedon, G., 1991. Forcing mechanisms of the Indian Ocean monsoon. Nature 353, 720–725.
Clemens, S.C., Prell, W.L., Sun, Y., 2010. Orbital-scale timing and mechanisms driving late Pleistocene Indo-Asian summer monsoons: reinterpreting cave speleothem δ18O. Paleoceanography 25, 1–19.
Clemens, S.C., Prell, W.L., Sun, Y., Liu, Z., Chen, G., 2008. Southern hemisphere forcing of pliocene δ18O and the evolution of indo–asian monsoons. Paleoceanography 23, 1–15.
Clemens, S.C., Tiedemann, R.F., 1997. Eccentricity forcing of Pliocene-Early Pleistocene climate revealed in a marine oxygen isotope record. Nature 385, 801–804.
Clemens, S.C., Yamamoto, M., Thirumalai, K., Giosan, L., Richey, J.N., Nilsson-Kerr, K., Rosenthal, Y., Anand, P., McGrath, S.M., 2021. Remote and local drivers of Pleistocene South Asian summer monsoon precipitation: a test for future predictions. Sci. Adv. 7 (23), eabg3848. https://doi.org/10.1126/sciadv.abg3848.
Clift, P.D., Hodges, K.V., Heslop, D., Hannigan, R., Long, V.H., Calves, A.G., 2008. Correlation of Himalayan exhumation rates and Asian monsoon intensity. Nat. Geosci. 1, 875–880.
Compo, G.P., Whitaker, J.S., Sardeshmukh, P.D., Matsui, N., Allan, R.J., Yin, X., Gleason, B.E., Vose, R.S., Rutledge, G., Bessemoulin, P., Brönnimann, S., Brunet, M., Crouthamel, R.I., Grant, A.N., Groisman, P.Y., Jones, P.D., Kruk, M., Kruger, A.C., Marshall, G.J., Maugeri, M., Mok, H.Y., Nordli, Ø., Ross, T.F., Trigo, R.M., Wang, X.L., Woodruff, S.D., Worley, S.J., 2011. The Twentieth Century reanalysis project. Q. J. R. Meteorol. Soc. 137, 1–28.
de Menocal, P., Bloemendal, J., King, J., 1991. A rock–magnetic record of monsoonal dust deposition to the Arabian Sea, Evidence for a shift in the mode of deposition at 2.4 Ma. Proc. ODP: Sci. Res. 117, 389–407. https://doi.org/10.2973/odp.proc.sr.117.178.1991.
Ding, Y., Chan, J., 2005. The East Asian summer monsoon: an overview. Meteorol. Atmos. Phys. 89, 117–142.
Ding, Y.H., Wang, Z.Y., Sun, Y., 2008. Inter-decadal variation of the summer precipitation in East China and its association with decreasing Asian summer monsoon. Part I: observed evidences. Int. J. Climatol. 28, 1139–1161.
Ding, Z., Derbyshire, E., Yang, S., Sun, J., Liu, T., 2005. Stepwise expansion of desert environment across northern China in the past 3.5 Ma and implications for monsoon evolution. Earth Planet Sci. Lett. 237, 45–55.
Ding, Z., Derbyshire, E., Yang, S., Yu, Z., Xiong, S., Liu, T., 2002. Stacked 2.6-Ma grain size record from the Chinese loess based on five sections and correlation with the deep-sea δ^{18}O record. Paleoceanography 17 (3).
Ding, Z., Liu, T., Rutter, N.W., Yu, Z., Guo, Z., Zhu, R., 1995. Ice–volume forcing of East Asian winter monsoon variations in the past 800,000 years. Quat. Res. 44, 149–159.
Ding, Z., Ren, J., Yang, S., Liu, T., 1999. Climate instability during the penultimate glaciation, Evidence from two high–resolution loess records, China. J. Geophy. Res. 104, 20123–20132.
Ding, Z., Yu, Z., Rutter, N.W., Liu, T., 1994. Towards an orbital time scale for Chinese loess deposits. Quat. Sci. Rev. 13 (1), 39–70.
Elderfield, H., Ferretti, P., Greaves, M., Crowhurst, S., McCave, I.N., Hodell, D.A., Piotrowski, A.M., 2012. Evolution of ocean temperature and ice volume through the mid-Pleistocene climate transition. Science 337, 704–709.
Elderfield, H., Ganssen, G., 2000. Past temperature and δ18O of surface ocean waters inferred from foraminiferal Mg/Ca ratios. Nature 405, 442–445. https://doi.org/10.1038/35013033.
Farrell, J.W., Janecek, T.R., 1991. Late neogene paleoceanography and paleoclimatology of the northeast Indian ocean (site 758). Proc. ODP: Sci. Res. 121, 297–355. https://doi.org/10.2973/odp.proc.sr.121.124.1991.
Felzer, B., Iii, T.W., Oglesby, R.J., 1998. The impact of ice sheets, CO2, and orbital insolation on late Quaternary climates: sensitivity experiments with a general circulation model. Quat. Sci. Rev. 17, 507–534.
France-Lanord, C., Spiess, V., Klaus, A., Schwenk, T., the Expedition 354 Scientists, 2016. Bengal Fan. Proceedings of the International Ocean Discovery Program, vol. 354. International Ocean Discovery Program, College Station, TX.
Fu, C., An, Z., Qiang, X., Bloemendal, J., Song, Y., Chang, H., 2013. Magnetostratigraphic determination of the age of ancient Lake Qinghai, and record of the east asian monsoon since 4.63 ma. Geology 41 (8), 875–878.
Gai, C., Liu, Q., Roberts, A.P., Chou, Y., Zhao, X., Jiang, Z., Liu, J., 2020. East Asian monsoon evolution since the late miocene from the south China sea. Earth Planet Sci. Lett. 530, 115960. https://doi.org/10.1016/j.epsl.2019.115960.
Gao, Y.X., Xu, S.Y., Guo, Q.Y., Zhang, M.L., 1962. Some Problems in the East Asian Monsoon. Chinese Science Press, Beijing, pp. 49–87.
Gebregiorgis, D., Hathorne, E.C., Giosan, L., Clemens, S., Nürnberg, D., Frank, M., 2018. Southern Hemisphere forcing of South Asian monsoon precipitation over the past ~1 Million years. Nat. Commun. 9, 4702. https://doi.org/10.1038/s41467-018-07076-2.
Geen, R., Bordoni, S., Battisti, D.S., Hui, K., 2020. Monsoons, ITCZs, and the concept of the global monsoon. Rev. Geophys. 58, e2020RG000700. https://doi.org/10.1029/2020RG000700.
Gordon, C., Cooper, C., Senior, C.A., Banks, H.T., Gregory, J.M., Johns, T.C., Mitchell, J.F.B., Wood, R.A., 2000. The simulation of SST, sea ice extents and ocean heat transports in a version of the Hadley Centre coupled model without flux adjustments. Clim. Dynam. 16, 147–168.
Guo, Z., Berger, A., Yin, Q., Qin, L., 2009. Strong asymmetry of hemispheric climates during MIS-13 inferred from correlating China loess and Antarctica ice records. Clim. Past 5, 21–31.
Guo, Z., Biscaye, P., Wei, L., Chen, X., Peng, S., Liu, T., 2000. Summer monsoon variations over the last 1.2 Ma from the weathering of loess-soil sequences in China. Geophys. Res. Lett. 27 (12), 1751–1754.
Guo, Z.T., Zhou, X., Wu, H.B., 2012. Glacial-interglacial water cycle, global monsoonand atmospheric methane changes. Clim. Dynam. 39, 1073–1092.
Han, W., Fang, X., Berger, A., 2012. Tibet forcing of mid–Pleistocene synchronous enhancement of East Asian winter and summer monsoons revealed by Chinese loess record. Quat. Res. 78, 174–184.
Han, Y., An, Z., Marlon, J.R., Bradley, R.S., Zhan, C., Arimoto, R., Sun, Y., Zhou, W., Wu, F., Wang, Q., Burr, G.S., Cao, J., 2020. Asian inland wildfires driven by

glacial–interglacial climate change. Proc. Natl. Acad. Sci. U.S.A. 117, 5184–5189. https://doi.org/10.1073/pnas.1822035117.
Hao, Q., Wang, L., Oldfield, F., Peng, S., Qin, L., Song, Y., Xu, B., Qiao, Y., Bloemendal, J., Guo, Z., 2012. Delayed build-up of Arctic ice sheets during 400,000-year minima in insolation variability. Nature 490, 392–396.
Hays, J.D., Imbrie, J., Shackleton, N.J., 1976. Variations in the Earth's orbit, pacemaker of the ice ages. Science 194, 1121–1132.
Head, M.J., Gibbard, P.L., 2015. Early–Middle Pleistocene transitions, linking terrestrial and marine realms. Quat. Int. 389, 7–46. https://doi.org/10.1016/j.quaint.2015.09.042.
Herbert, T.D., Peterson, L.C., Lawrence, K.T., Liu, Z., 2010. Tropical ocean temperatures over the past 3.5 Million years. Science 328, 1530–1534.
Heslop, D., Dekkers, M.J., Langereis, C.G., 2002. Timing and structure of the mid–Pleistocene transition, records from the loess deposits of northern China. Palaeogeogr. Palaeoclimatol. Palaeoecol. 185, 133–143.
Hodell, D.A., Channell, J.E.T., Curtis, J.H., Romero, O., Röhl, U., 2008. Onset of "hudson strait" heinrich events in the eastern North Atlantic at the end of the middle pleistocene transition (~640 ka). Paleoceanography 23, PA4218.
Hönisch, B., Hemming, N.G., Archer, D., Siddall, M., McManus, J.F., 2009. Atmospheric carbon dioxide concentration across the mid-Pleistocene transition. Science 324, 1551–1554.
Imbrie, J., Imbrie, K., 1979. Ice Ages: Solving the Mystery. Enslow Publishers, New Jersey, pp. 1–224.
Irino, T., Tada, R., Ikehara, K., Sagawa, T., Karasuda, A., Kurokawa, S., Seki, A., Lu, S., 2018. Construction of perfectly continuous records of physical properties for dark-light sediment sequences collected from the Japan sea during integrated ocean drilling program expedition 346 and their potential utilities as paleoceanographic studies. Prog. Earth Planet. Sci. 5 (1), 23.
Jansen, J.H.F., Kuijpers, A., Troelstra, S.R., 1986. A mid-Brunhes climatic event: long term changes in global atmosphere and ocean circulation. Science 232, 619–622.
Jian, Z., Huang, B., Kuhnt, W., Lin, H., 2001. Late quaternary upwelling intensity and East asian monsoon forcing in the south China sea. Quat. Res. 55, 363–370.
Jiang, D.B., Wang, H.J., Lang, X.M., 2005. Evaluation of East Asian climatology as simulated by seven coupled models. Adv. Atmos. Sci. 22, 479–495.
Jiang, F., Fu, J., Wang, S., Sun, D., Zhao, Z., 2007. Formation of the Yellow River, inferred from loess-palaeosol sequence in Mangshan and lacustrine sediments in Sanmen gorge, China. Quat. Int. 175 (12), 62–70.
Kukla, G., Heller, F., Liu, X.M., Xu, T.C., Liu, T.S., An, Z., 1988. Pleistocene climate in China dated by magnetic susceptibility. Geology 16, 811–814.
Kunkelova, T., Jung, S.J.A., de Leau, E.S., Odling, N., Thomas, A.L., Betzler, C., Eberli, G.P., Alvarez-Zarikian, C.A., Alonso-García, M., Bialik, O.M., Blättler, C.L., Guo, J.A., Haffen, S., Horozal, S., Mee, A.L.H., Inoue, M., Jovane, L., Lanci, L., Laya, J.C., Lüdmann, T., Bejugam, N.N., Nakakuni, M., Niino, K., Petruny, L.M., Pratiwi, S.D., Reijmer, J.J.G., Reolid, J., Slagle, A.L., Sloss, C.R., Su, X., Swart, P.K., Wright, J.D., Yao, Z., Young, J.R., Lindhorst, S., Stainbank, S., Rueggeberg, A., Spezzaferri, S., Carrasqueira, I., Yu, S., Kroon, D., 2018. A two million year record of low-latitude aridity linked to continental weathering from the Maldives. Prog. Earth Planet. Sci. 5 (1), 86. https://doi.org/10.1186/s40645-018-0238-x.
Kutzbach, J.E., Guetter, P.J., 1986. The influence of changing orbital parameters and surface boundary conditions on climate simulations for the past 18 000 years. J. Atmos. Sci. 43, 1726–1759.
Kutzbach, J.E., Liu, X., Liu, Z., Chen, G., 2008. Simulation of the evolutionary response of global summer monsoons to orbital forcing over the past 280,000 years. Clim. Dynam. 30, 567–579. https://doi.org/10.1007/s00382-007-0308-z.
Kutzbach, J.E., Otto-Bliesner, B.L., 1982. The sensitivity of the african-asian monsoonal climate to orbital parameter changes for 9000 Years B.P. In a low-resolution general circulation model. J. Atmos. Sci. 39, 1177–1188.
Lee, J., Kim, S., Khim, B.-K., 2020. A paleoproductivity shift in the northwestern Bay of Bengal (IODP Site U1445) across the mid-Pleistocene transition in response to weakening of the Indian summer monsoon. Palaeogeogr. Palaeoclimatol. Palaeoecol. 560, 110018. https://doi.org/10.1016/j.palaeo.2020.110018.
Lei, Y.H., Hoskins, B., Slingo, J., 2014. Natural variability of summer rainfall over China in HadCM3. Clim. Dynam. 42, 417–432.
Li, B., Feng, Q., Wang, F., Wang, X., Li, R., 2019a. A 1.68 Ma organic isotope record from the hetao basin, upper reaches of the Yellow River in northern China: implications for hydrological and ecological variations. Global Planet. Change 184, 103061.
Li, J., Fang, X., Song, C., Pan, B., Ma, Y., Yan, M., 2014a. Late Miocene–Quaternary rapid stepwise uplift of the NE Tibetan Plateau and its effects on climatic and environmental changes. Qual. Res. 81, 400–423.
Li, L., Li, Q., Tian, J., Wang, P., Wang, H., Liu, Z., 2011. A 4–Ma record of thermal evolution in the tropical western Pacific and its implications on climate change. Earth Planet Sci. Lett. 309, 10–20.
Li, M., Hinnov, L., Kump, L., 2019b. Acycle: time-series analysis software for paleoclimate research and education. Comput. Geosci. 127, 12–22. https://doi.org/10.1016/j.cageo.2019.02.011.
Li, T., Li, G., 2014. Incorporation of trace metals into microcodium as novel proxies for paleo–precipitation. Earth Planet Sci. Lett. 386, 34–40. https://doi.org/10.1016/j.epsl.2013.10.011.
Li, T., Liu, F., Abels, H.A., You, C., Zhang, Z., Chen, J., Ji, J., Li, L., Li, L., Liu, H., Ren, C., Xia, R., Zhao, L., Zhang, W., Li, G., 2016. Continued obliquity pacing of East Asian summer precipitation after the mid–Pleistocene transition. Earth Planet Sci. Lett. 457, 181–190. https://doi.org/10.1016/j.epsl.2016.09.045.
Li, Y., Lu, R.Y., Dong, B.W., 2007. The ENSO–Asian monsoon interaction in acoupled ocean–atmosphere GCM. J. Clim. 20, 5164–5177.
Li, Z.J., Sun, D.H., Chen, F.H., Nie, J.S., Wang, F., Zhang, Y.B., Guo, F., Wang, X., Li, B.F., 2014b. Chronology studies of a drill core in the central Tengger Desert of China and its paleoclimatic implications. Quat. Sci. Rev. 85, 85–98.
Liang, X.Z., Sun, C., Zheng, X., Dai, Y.J., Xu, M., Choi, H.I., Ling, T.J., Qiao, F.X., Kong, X.H., Bi, X.Q., Song, L.C., Wang, F., 2019. CWRF performance at downscaling China climate characteristics. Clim. Dynam. 52, 2159–2184.
Lisiecki, L.E., Raymo, M.E., 2005. A Pliocene–Pleistocene stack of 57 globally distributed benthic δ18O records. Paleoceanography 20, 1–17.
Liu, C.Y., Nie, J.S., Li, Z.J., Qiao, Q.Q., Abelle, J., Wang, F., Xiao, W.J., 2021. Eccentricity forcing of East Asian monsoonal systems over the past 3 million years. Proc. Natl. Acad. Sci. U.S.A. 1182 (118), e2107055118.
Liu, J., Liu, Q., Zhang, X., Liu, J., Wu, Z., Mei, X., Shi, X., Zhao, Q., 2016. Magnetostratigraphy of a long Quaternary sediment core in the south Yellow Sea. Quat. Sci. Rev. 144, 1–15.
Liu, T., Ding, Z., 1998. Chinese loess and the paleomonsoon. Annu. Rev. Earth Planet Sci. 26, 111–145.
Liu, T., Ding, Z., Rutter, N., 1999. Comparison of Milankovitch periods between continental loess and deep sea records over the last 2.5 Ma. Quat. Sci. Rev. 18, 1205–1212. S0277-3791(98)00110-3.
Liu, W., Yang, H., Sun, Y., Wang, X., 2011. δ^{13}C values of loess total carbonate, a sensitive proxy for Asian summer monsoon in arid northwestern margin of the Chinese loess plateau. Chem. Geol. 284, 317–322. https://doi.org/10.1016/j.chemgeo.2011.03.011.
Liu, Z., Wen, X., Brady, E.C., Otto–Bliesner, B., Yu, G., Lu, H., Cheng, H., Wang, Y., Zheng, W., Ding, Y., Edwards, R.L., Cheng, J., Liu, W., Yang, H., 2014. Chinese cave records and the East Asia summer monsoon. Quat. Sci. Rev. 83, 115–128.
Lu, H.X., Liu, W.G., Yang, H., Wang, H.Y., Liu, Z.H., Leng, Q., Sun, Y.B., Zhou, W.J., An, Z.S., 2019. 800-kyr land temperature variations modulated by vegetation changes on Chinese Loess Plateau. Nat. Commun. 10, 1530–1534.
Lu, H., Liu, X., Zhang, F., An, Z., Dodson, J., 1999. Astronomical calibration of loess–paleosol deposits at Luochuan, central Chinese loess plateau. Palaeogeogr. Palaeoclimatol. Palaeoecol. 154, 237–246. https://doi.org/10.1016/S0031-0182(99)00113-3.
Lü, H., Wang, S., Wu, N., Tong, G., Yang, X., Shen, C., Li, S., Zhu, L., Wang, L., 2001. A new pollen record of the last 2.8 Ma fromthe Co Ngoin, central Tibetan Plateau. Sci. China, Ser. A D 44, 292–300. Supp.).
Lu, H., Wang, X., Wang, X., Sun, X., Yi, S., Zhou, Y., Liu, Q., Swinehart, J., Vandenberghe, J., 2012. Palaeoclimatic changes in northeastern Qinghai-Tibetan Plateau revealed by magnetostratigraphy and magnetic susceptibility analysis of thick loess deposits. Neth. J. Gersci. (Geologie en Mijnbouw) 91 (1–2), 189–198.
Lu, H., Yi, S., Liu, Z., Mason, J.A., Jiang, D., Cheng, J., Stevens, T., Xu, E., Jin, L., Zhang, Z., Guo, Z., Wang, Y., Otto–Bliesner, B., 2013. Variation of East Asian monsoon precipitation during the past 21 k.y. and potential CO_2 forcing. Geology 41, 1023–1026.
Lu, H., Zhang, F., Liu, X., Duce, R.A., 2004. Periodicities of palaeoclimatic variations recorded by loess–paleosol sequences in China. Quat. Sci. Rev. 23, 1891–1900.
Lüthi, D., Le Floch, M., Bereiter, B., Blunier, T., Barnola, J.M., Siegenthaler, U., Raynaud, D., Jouzel, J., Fishcher, H., Kawamura, K., Stocker, T.F., 2008. High-resolution carbon dioxide concentration record 650 00–800 000 years before present. Nature 453, 379–382.
Lyu, A., Yin, Q., Crucifix, M., Sun, Y., 2021. Diverse regional sensitivity of summer precipitation in East Asia to ice volume, CO_2 and astronomical forcing. Geophys. Res. Lett. 48, e2020GL092005. https://doi.org/10.1029/2020GL092005.
Maher, B.A., 2016. Palaeoclimatic records of the loess/palaeosol sequences of the Chinese Loess Plateau. Quat. Sci. Rev. 154, 23–84.
Maher, B.A., Thompson, R., 1995. Paleorainfall reconstructions from pedogenic magnetic susceptibility variations in the Chinese loess and paleosols. Quat. Res. 44, 383–391.
Miao, Y., Warny, S., Liu, C., Clift, P.D., Gregory, M., 2017. Neogene fungal record from IODP site U1433, South China Sea: implications for paleoenvironmental change and the onset of the Mekong River. Mar. Geol. 394, 69–81.
Milankovitch, M., 1941. Canon of insolation and the ice–age problem. R. Serb. Acad. Spec. Publ. (translated by the Israel Program for Scientific Translations, Jerusalem, 1969).
Müller, P.J., Kirst, G., Ruhland, G., Storch, I.V., Rosell-Mele, A., 1998. Calibration of the Alkenone paleotemperature index UK37 based on core-tops from the eastern South Atlantic and the global ocean (60° N–60° S). Geochem. Cosmochim. Acta 62, 1757–1772.
Naafs, B.D.A., Hefter, J., Stein, R., 2013. Millennial-scale ice rafting events and Hudson Strait Heinrich (-like) events during the late Pliocene and Pleistocene: a review. Quat. Sci. Rev. 80, 1–28.
Nie, J., Stevens, T., Rittner, M., Stockli, D., Garzanti, E., Limonta, M., Bird, A., Ando, S., Vermeesch, P., Saylor, J., Lu, H., Breecker, D., Hu, X., Liu, S., Resentini, A., Vezzoli, G., Peng, W., Carter, A., Ji, S., Pan, B., 2015. Loess Plateau storage of northeastern tibeta plateau-derived Yellow River sediment. Nat. Commun. 6, 8511.
Oakley, J.E., O'Hagan, A., 2004. Probabilistic sensitivity analysis of complex models: a Bayesian approach. J. Roy. Stat. Soc. B 66, 751–769.
Pandey, D.K., Clift, P.D., Kulhanek, D.K., and the Expedition 355 Scientists, 2016. Arabian Sea Monsoon. Proceedings of the International Ocean Discovery Program, vol. 355. International Ocean Discovery Program, College Station, TX. https://doi.org/10.14379/iodp.proc.355.2016.
Peterse, F., Martínez-García, A., Zhou, B., Beets, C.J., Prins, M.A., Zheng, H.,

Eglintonet, T.I., 2014. Molecular records of continental air temperature and monsoon precipitation variability in East Asia spanning the past 130,000 years. Quat. Sci. Rev. 83, 76–82.
Petit, J.R., Jouzel, J., Raynaud, D., Barkov, N., Barnola, J.M., Basile, I., Bender, M., Chappellaz, J., Davisk, M., Delaygue, G., Delmotte, M., Kotlyakov, V.M., Legrand, M., Lipenkov, V.Y., Lorius, C., Pepin, L., Riz, C., Saltzmank, E., Stievenard, M., 1999. Climate and atmospheric history of the past 420,000 years from the Vostok ice core, Antarctica. Nature 399, 429–436.
Pisias, N.G., Moore, T.C., 1981. The evolution of Pleistocene climate, a time series approach. Earth Planet Sci. Lett. 52, 450–458.
Prell, W.L., Kutzbach, J.E., 1987. Monsoon variability over the past 150,000 years. J. Geophys. Res. 92, 8411–8425.
Prell, W.L., Kutzbach, J.E., 1992. Sensitivity of the Indian monsoon to forcing parameters and implications for its evolution. Nature 360, 647–652.
Raymo, M.E., Oppo, D.W., Curry, W., 1997. The mid–Pleistocene climate transition: a deep sea carbon isotopic perspective. Paleoceanography 12, 546–559.
Rits, D.S., Prins, M.A., Troelstra, S.R., Balen, R.T.V., Zheng, Y., Beets, C.J., Wang, B., Li, X., Zhou, J., Zheng, H., 2016. Facies analysis of the middle and late quaternary sediment infill of the northern weihe basin, central China. J. Quat. Sci. 31, 152–165.
Rohling, E.J., 2007. Progress in paleosalinity: overview and presentation of a new approach. Paleoceanography 22, PA3215.
Rohling, E.J., Foster, G.L., Grant, K.M., Marino, G., Roberts, A.P., Tamisiea, M.E., Williams, F., 2014. Sea–level and deep–sea–temperature variability over the past 5.3 million years. Nature 508, 477–482.
Ruddiman, W.F., Raymo, M., McIntyre, A., 1986. Matuyama 41,000-year cycles: north Atlantic Ocean and northern hemisphere ice sheets. Earth Planet Sci. Lett. 80, 117–129.
Shackleton, N.J., 2000. The 100,000–year ice–age cycle identified and found to lag temperature, carbon dioxide, and orbital eccentricity. Science 289, 1897–1902.
Shackleton, N.J., Opdyke, N.D., 1976. Oxygen-isotope and paleomagnetic stratigraphy of Pacific core V28-239 late Pliocene to latest Pleistocene. In: Cune, R.M., Hays, J.D. (Eds.), Investigation of Late Quaternary Paleoceanography and Paleoclimatology. Bremerhaven. Geological Society of America, pp. 449–464.
Shen, C., Tang, L., Wang, S., Li, C., Liu, K.B., 2005. Pollen records and time scale for the RM core of the Zoige Basin, northeastern Qinghai-Tibetan Plateau. Chin. Sci. Bull. 50, 553–562.
Shen, J., Lu, H., Wang, S., Chen, S., Yang, X., Wu, Y., Zhu, Z., 2004. A 2.8 Ma record of environmental evolution and tectonic events inferred from the Cuoe core in the middle of Tibetan Plateau. Sci. China, Ser. A D 47 (11), 1025–1034.
Shen, J., Xiao, H., Wang, S., An, Z., Qiang, X., Xiao, X., 2007. The orbital scale evolution of regional climate recorded in a long sediment core from Heqing, China. Chin. Sci. Bull. 52, 1813–1819.
Shi, F., Duan, A., Yin, Q.Z., Bruun, J., Xiao, C., Guo, Z.T., 2021a. Modulation of the relationship between summer temperatures in the Qinghai–Tibetan Plateau and Arctic over the past millennium by external forcings. Quat. Res. 103, 1–9.
Shi, F., Yin, Q.Z., Nikolova, I., Berger, A., Ramstein, G., Guo, Z.T., 2021b. Impacts of extremely asymmetrical polar ice sheets on the East Asian summer monsoon during the MIS-13 interglacial. Quat. Sci. Rev. 231, 106164.
Shi, X., Yao, Z., Liu, Q., Larrasoaña, J.C., Bai, Y., Liu, Y., Liu, J., Cao, P., Li, X., Qiao, S., Wang, K., Fang, X., Xu, T., 2016. Sedimentary architecture of the bohai sea China over the last 1 ma and implications for sea-level changes. Earth Planet Sci. Lett. 451, 10–21.
Shi, Z.G., Liu, X.D., Sun, Y.B., An, Z.S., Liu, Z.Y., Kutzbach, J., 2011. Distinct responses of East Asian summer and winter monsoons to orbital forcing. Clim. Past 7, 1363–1370.
Singarayer, J.S., Valdes, P.J., 2010. High-latitude climate sensitivity to ice-sheet forcing over the last 120 kyr. Quat. Sci. Rev. 29, 43–55.
Slivinski, L.C., Compo, G.P., Whitaker, J.S., Sardeshmukh, P.D., Giese, B.S., McColl, C., Allan, R., Yin, X., Vose, R., Titchner, H., Kennedy, J., Spencer, L.J., Ashcroft, L., Brönnimann, S., Brunet, M., Camuffo, D., Cornes, R., Cram, T.A., Crouthamel, R., Domínguez-Castro, F., Freeman, J.E., Gergis, J., Hawkins, E., Jones, P.D., Jourdain, S., Kaplan, A., Kubota, H., Le Blancq, F., Lee, T., Lorrey, A., Luterbacher, J., Maugeri, M., Mock, C.J., Moore, G.K., Przybylak, R., Pudmenzky, C., Reason, C., Slonosky, V.C., Smith, C., Tinz, B., Trewin, B., Valente, M.A., Wang, X.L., Wilkinson, C., Wood, K., Wyszyński, P., 2019. Towards a more reliable historical reanalysis: improvements for version 3 of the Twentieth Century Reanalysis system. Quart. J. Roy. Meteor. Soc. 145, 2876–2908.
Song, Y., Fang, X., King, J.W., Li, J., Naoto, I., An, Z., 2014. Magnetic parameter variations in the Chaona loess/paleosol sequences in the central Chinese Loess Plateau, and their significance for the middle Pleistocene climate transition. Quat. Res. 81, 433–444.
Sun, J., Liu, T., 2000a. Stratigraphic evidence for the uplift of the Tibetan Plateau between ~1.1 and ~0.9 Myr ago. Quat. Res. 54, 309–320.
Sun, J., Liu, T., 2000b. Multiple origins and interpretations of the magnetic susceptibility signal in Chinese wind-blown sediments. Earth Planet Sci. Lett. 180, 287–296.
Sun, J., 2005. Long-termfluvial archives in the Fen Wei Graben, central China, and their bearing on the tectonic history of the India–Asia collision system during the Quaternary. Quat. Sci. Rev. 24, 1279–1286.
Sun, Y., An, Z., Clemens, S.C., Bloemendal, J., Vandenberghe, J., 2010. Seven million years of wind and precipitation variability on the Chinese Loess Plateau. Earth Planet Sci. Lett. 297, 525–535.
Sun, Y., Clemens, S.C., An, Z., Yu, Z., 2006a. Astronomical timescale and palaeoclimatic implication of stacked 3.6–Myr monsoon records from the Chinese Loess Plateau. Quat. Sci. Rev. 25, 33–48.
Sun, Y., Chen, J., Clemens, S.C., Liu, Q., Ji, J., Tada, R., 2006b. East Asian monsoon variability over the last seven glacial cycles recorded by a loess sequence from the northwestern Chinese Loess Plateau. G-cubed 7, Q12Q02.
Sun, Y., Kutzbach, J., An, Z., Clemens, S., Liu, Z., Liu, W., Liu, X., Shi, Z., Zheng, W., Liang, L., Yan, Y., 2015. Astronomical and glacial forcing of East Asian summer monsoon variability. Quat. Sci. Rev. 115, 132–142. https://doi.org/10.1016/j.quascirev.2015.03.009.
Sun, Y., McManus, J.F., Clemens, S.C., Zhang, X., Vogel, H., Hodel, D.A., Guo, F., Wang, T., Liu, X., An, Z., 2021. Persistent orbital influence on millennial climate variability through the Pleistocene. Nat. Geosci. https://doi.org/10.1038/s41561-021-00794-1.
Sun, Y., Yin, Q., Crucifix, M., Clemens, S.C., Araya–Melo, P., Liu, W., Qiang, X., Liu, Q., Zhao, H., Liang, L., Chen, H., Li, Y., Zhang, L., Dong, G., Li, M., Zhou, W., Berger, A., An, Z., 2019. Diverse manifestations of the mid–Pleistocene climate transition. Nat. Commun. 10, 1–11.
Tada, R., Koizumi, I., Cramp, A., Rahman, A., 1992. Correlation of dark and light layers, and the origin of their cyclicity in the Quaternary sediments from the Japan Sea. Proc. Ocean Drill. Progr. Sci. Results 127/128, 577–601.
Tada, R., Irino, T., Ikehara, K., Karasuda, A., Sugisaki, S., Xuan, C., Sagawa, T., Itaki, T., Kubota, Y., Lu, S., Seki, A., Murray, R.W., Alvarez-Zarikian, C., Anderson, W.T., Bassetti, M.-A., Brace, B.J., Clemens, S.C., da Costa Gurgel, M.H., Dickens, G.R., Dunlea, A.G., Gallagher, S.J., Giosan, L., Henderson, A.C.G., Holbourn, A.E., Kinsley, C.W., Lee, G.S., Lee, K.E., Lofi, J., Lopes, C.I.C.D., Saavedra-Pellitero, M., Peterson, L.C., Singh, R.K., Toucanne, S., Wan, S., Zheng, H., Ziegler, M., 2018. High-resolution and high-precision correlation of dark and light layers in the Quaternary hemipelagic sediments of the Japan Sea recovered during IODP Expedition 346. Prog. Earth Planet. Sci. 5 (1), 19.
Tada, R., Murray, R.W., Alvarez Zarikian, C.A., and the Expedition 346 Scientists, 2015. Proceedings of the International Ocean Discovery Program, vol. 346. https://doi.org/10.2204/iodp.proc.346.2015. College Station, TX (Integrated Ocean Drilling Program).
Tian, J., Wang, P., Cheng, X., Li, Q., 2002. Astronomically tuned plio–pleistocene benthic δ18O record from south China sea and atlantic–pacific comparison. Earth Planet Sci. Lett. 203, 1015–1029.
Tian, J., Xie, X., Ma, W., Jin, H., Wang, P., 2011. X–ray fluorescence core scanning records of chemical weathering and monsoon evolution over the past 5 Myr in the southern South China Sea. Paleoceanography 26, 1–17.
Thomas, E.K., Clemens, S.C., Sun, Y.B., Prell, W.L., Huang, Y., Gao, L., Loomis, S., Chen, G., Liuet, Z., 2016. Heterodynes dominate precipitation isotopes in the East Asian monsoon region, reflecting interaction of multiple climate factors. Earth Planet Sci. Lett. 455, 196–206.
Wang, B., 2006. The Asian Monsoon. Springer/Praxis, New York, p. 787.
Wang, B., Ding, Q., 2008. Global monsoon: dominant mode of annual variation in the tropics. Dynam. Atmos. Oceans 44, 165–183.
Wang, P., Jian, Z., Zhao, Q., Li, Q., Wang, R., Liu, Z., Wu, G., Shao, L., Wang, J., Huang, B., Fang, D., Tian, J., Li, J., Li, X., Wei, G., Sun, X., Luo, Y., Su, X., Mao, S., Chen, M., 2003. Evolution of the South China Sea and monsoon history revealed in deep-sea records. Chin. Sci. Bull. 48, 2549–2561.
Wang, P.X., Clemens, S., Beaufort, L., Braconnot, P., Dickens, G.R., Huber, M., Jian, Z.M., Kershaw, P., Sarnthein, M., 2005. Evolution and variability of the Asian monsoon system: state of the art and outstanding issues. Quat. Sci. Rev. 24, 595–629.
Wang, P., Prell, W.L., Blum, P., Shipboard Scientific Party, 2000. Proceedings of the Ocean Drilling Program, Initial Reports, vol. 184. Ocean Drilling Program), College Station, TX. https://doi.org/10.2973/odp.proc.ir.184.106.2000.
Wang, P., Wang, B., Cheng, H., Fasullo, J., Guo, Z., Kiefer, T., Liu, Z., 2014. The global monsoon across timescales, coherent variability of regional monsoons. Clim. Past 10, 2007–2052.
Wang, P., Wang, B., Cheng, H., Fasullo, J., Guo, Z., Kiefer, T., Liu, Z., 2017. The global monsoon across time scales, mechanisms and outstanding issues. Earth Sci. Rev. 174, 84–121. https://doi.org/10.1016/j.earscirev.2017.07.006.
Wang, F., Sun, D., Chen, F., Bloemendal, J., Guo, F., Li, Z., Zhang, Y., Li, B., Wang, X., 2015. Formation and evolution of the Badain Jaran Desert, North China, as revealed by a drill core from the desert center and by geological survey. Palaeogeogr. Palaeoclimatol. Palaeoecol. 426, 139–158.
Wang, Y., Cheng, H., Edwards, R., An, Z., Wu, J., Shen, C., Dorale, J., 2001. A high-resolution absolute-dated late Pleistocene monsoon record from Hulu Cave, China. Science 294, 2345–2348.
Wang, Y., Cheng, H., Edwards, R.L., Kong, X., Shao, X., Chen, S., Wu, J., Jiang, X., Wang, X., An, Z., 2008. Millennial–and orbital–scale changes in the East Asian monsoon over the past 224,000 years. Nature 451, 1090–1093.
Webster, P.J., Magana, V.O., Palmer, T.N., Shukla, J., Tomas, R.A., Yanai, M.U., Yasunari, T., 1998. Monsoons, processes, predictability, and the prospects for prediction. J. Geophys. Res. Oceans 103, 14451–14510.
Wehausen, R., Brumsack, H., 2002. Astronomical forcing of the east asian monsoon mirrored by the composition of pliocene south China sea sediments. Earth Planet Sci. Lett. 201, 621–636.
Wei, G., Li, X., Liu, Y., Shao, L., Liang, X., 2006. Geochemical record of chemical weathering and monsoon climate change since the early Miocene in the South China Sea. Paleoceanography 21, PA4214.
Wen, X., Liu, Z., Wang, S., Cheng, J., Zhu, J., 2016. Correlation and anti-correlation of the East Asian summer and winter monsoons during the last 21,000 years. Nat. Commun. 7, 11999. https://doi.org/10.1038/ncomms11999.
Williams, D.F., Kuzmin, M.I., Prokopenko, A.A., Karabanov, E.B., Khursevich, G.K.,

Bezrukova, E.V., 2001. The Lake Baikal drilling project in the context of a global lake drilling initiative. Quat. Int. 80, 3–18. https://doi.org/10.1016/S1040-6182(01)00015-5.
Xiao, J., An, Z., 1999. Three large shifts in East Asian monsoon circulation indicated by loess–paleosol sequences in China and late Cenozoic deposits in Japan. Palaeogeogr. Palaeoclimatol. Palaeoecol. 154, 179–189.
Xiao, J., Zheng, H., Zhao, H., 1992. Variation of winter monsoon intensity on the Loess Plateau, central China during the last 130,000 years, evidences from grain size distribution. Quat. Res. 31, 13–19.
Xin, S., Shen, J., Zhang, W., Sun, W., Xiao, X., 2019. East Asian winter monsoon evolution since the late Pliocene based on a pollen record from Lake Xingkai, northeast Asia. Quat. Res. 93, 40–59.
Xiong, S., Ding, Z., Liu, T., 2001. Climatic implications of loess deposits from the Beijing region. J. Quat. Sci. 6, 575–582.
Yang, S., Ding, Z., Li, Y., Wang, X., Jiang, W., Huang, X., 2015. Warming-induced northwestward migration of the east Asian monsoon rain belt from the last glacial maximum to the mid-Holocene. P. Natl. Acad. Sci. USA 112, 13178–13183.
Yi, L., Deng, C., Tian, L., Xu, X., Jiang, X., Qiang, X., Qin, H., Ge, J., Chen, G., Su, Q., Chen, Y., Shi, X., Xie, Q., Yu, H., Zhu, R., 2016. Plio-Pleistocene evolution of Bohai basin (East Asia): demise of Bohai Paleolake and transition to marine environment. Sci. Rep. 6, 29403.
Yin, Q., Berger, A., Crucifix, M., 2009. Individual and combined effects of ice sheets and precession on MIS-13 climate. Clim. Past 5, 229–243.
Yin, Q., Berger, A., Driesschaert, E., Goosse, H., Loutre, M.F., Crucifix, M., 2008. The eurasian ice sheet reinforces the East Asian summer monsoon during the interglacial 500 000 years ago. Clim. Past 4 (2), 80–90.
Zachos, J., Pagani, M., Sloan, L., Thomas, E., Billups, K., 2001. Trends, rhythms, and aberrations in global climate 65 Ma to present. Science 292, 686–693.
Zeng, L., Lu, H., Yi, S., Li, Y., Lv, A., Zhang, W., Xu, Z., Wu, H., Feng, H., Cui, M., 2016. New magnetostratigraphic and pedostratigraphic investigations of loess deposits in north-east China and their implications for regional environmental change during the mid-pleistocene climatic transition. J. Quat. Sci. 31 (1), 20–32.
Zhang, C., Zhao, C., Yu, S.Y., Yang, X.D., Cheng, J., Zhang, X.J., Xue, B., Shen, J., Chen, F.H., 2022. Seasonal imprint of Holocene temperature reconstruction on the Tibetan Plateau. Earth Sci. Rev. 226, 103927.
Zhang, H.B., Griffiths, M.L., Chiang, J.C.H., Kong, W.W., Wu, S.T., Atwood, A., Huang, J.H., Cheng, H., Ning, Y.F., Xie, S.C., 2018a. East Asian hydroclimate modulated by the position of the westerlies during Termination I. Science 362, 580–583.
Zhang, H.B., Nie, J.S., Liu, X.J., Pullen, A., Li, G.Q., Peng, W.B., Zhang, H.Z., 2021. Spatially variable provenance of the Chinese Loess Plateau. Geology 49 (10), 1155–1159.
Zhang, J., Li, J., Guo, B., Ma, Z., Li, X., Ye, X., Yu, H., Liu, J., Yang, C., Zhang, S., Song, C., Hui, Z., Peng, T., 2016. Magnetostratigraphic age and monsoonal evolution recorded by the thickest quaternary loess deposit of the Lanzhou region, western Chinese Loess Plateau. Quat. Sci. Rev. 139, 17–29.
Zhang, W., De Vleeschouwer, D., Shen, J., Zhang, Z., Zeng, L., 2018b. Orbital time scale records of asian eolian dust from the Sea of Japan since the early pliocene. Quat. Sci. Rev. 187, 157–167.
Zhang, Y., Ji, J., Balsam, W.L., Liu, L., Chen, J., 2007. High resolution hematite and goethite records from ODP 1143, South China Sea, co–evolution of monsoonal precipitation and El Niño over the past 600,000 years. Earth Planet Sci. Lett. 264, 136–150.
Zhang, Y., Ji, J., Balsam, W.L., Liu, L., Chen, J., 2009. Mid–Pliocene asian monsoon intensification and the onset of northern hemisphere glaciation. Geology 37, 599–602.
Zhao, Y., Tzedakis, P.C., Li, Q., Qin, F., Cui, Q., Liang, C., Birks, H.B., Liu, Y.L., Zhang, Z.Y., Ge, J.Y., Zhao, H., Felde, V.A., Deng, C.L., Cai, M.T., Li, H., Ren, W.H., Wei, H.C., Yang, H.F., Zhang, J.W., Yu, Z.C., Guo, Z., 2020. Evolution of vegetation and climatevariability on the Tibetan Plateau over the past 1.74 million years. Sci. Adv. 6, eaay6193.
Zheng, H., An, Z., Shaw, J., 1992. New contributions to Chinese Plio-Pleistocene magnetostratigraphy. Phys. Earth Planet. In. 70, 146–153.
Zheng, H., Huang, X., Ji, J., Rui, L., Zeng, Q., Jiang, F., 2007. Ultra-high rates of loess sedimentation at Zhengzhou since stage 7: implication for the yellow river erosion of the Sanmen gorge. Geomorphology 85, 131–142.
Zheng, Y.Q., Yu, G., Wang, S.M., Xue, B., Zhou, D.Q., Zeng, X.M., Liu, H.Q., 2004. Simulation of paleoclimate over East Asia at 6ka BP and 21ka BP by a regional climate model. Clim. Dynam. 23, 513–529.
Zhou, L., Oldfield, F., Wintle, A.G., Robinson, S.G., Wang, J., 1990. Partly pedogenic origin of magnetic variations in Chinese loess. Nature 346, 737–739.
Ziegler, M., Lourens, L.J., Tuenter, E., Hilgen, F., Reichart, G.J., Weber, N., 2010. Precession phasing offset between Indian summer monsoon and Arabian Sea productivity linked to changes in Atlantic overturning circulation. Paleoceanography 25, 1–16. https://doi.org/10.1029/2009PA001884. PA3213.